# Non-Local Effects of Support Structure Diameter on Wave Induced Fatigue Loads of Monopile-based Offshore Wind Turbines

FRANCESCO CASTELLINO

December 2, 2022

TUDelft Delft University of Technology

NTNU

SIEMENS Gamesa RENEWABLE ENERGY

# Non-Local Effects of Support Structure Diameter on Wave Induced Fatigue Loads of Monopile-based Offshore Wind Turbines

**Master of Science Thesis**

| | | |
|---|---|---|
| *Author:* | FRANCESCO CASTELLINO | |
| *Committee:* | Dr. Ir. P. van der Male | TU Delft - Chairman |
| | Dr. Ir. H. Hendrikse | TU Delft |
| | Prof. M. Muskulus | NTNU |
| | Prof. Z. Ghao | NTNU |
| | Ir. J. Daamen | Siemens Gamesa RE |

**December 2, 2022**

- CONFIDENTIAL -

# Summary

One of the main cost drivers of an offshore wind power plant are the support structures of the wind turbines, it is therefore of primary importance to optimize their design. Among the support structures available, the concept most widely adopted is the monopile-based support structure, whose design is often fatigue-driven. Offshore structures need to withstand the wave loads, that play a major role among the cyclic loads that excite the support structure. The design of the support structure's geometry is of primary importance, since it determines the structural vibrations.

Therefore, this thesis aims to understand how, varying the diameter of the support structure, affects the wave induced fatigue loads acting on a monopile-based offshore wind turbine. A FE model was developed to represent the structural motion, where the Euler-Bernoulli beam theory was adopted. The linear wave theory was used, and the wave loads were computed according to the Morison equation. The wave induced fatigue loads were calculated in frequency domain, assuming a narrow-banded response spectrum. A case study was provided by Siemens Gamesa RE, and the wind turbine was assumed in parked mode.

Two assignments were derived, to tackle the research question. First, a sensitivity analysis was performed, to study the non-local effects on the wave induced loads, due to varying the diameter of the support structure. Then, an analytical optimization was applied to a simplified structure, aiming to find the diameter that minimizes the mass of the support structure, accounting for fatigue damage. The hypotheses of thin wall and deep water regime were assumed.

The results of the sensitivity analysis suggested that the non-local effects do not differ significantly from the local ones, and that to reduce the loads: it is beneficial to reduce the diameter at waterline, to increase it around mudline, while variations along the tower are quite irrelevant to this end. The analytical optimization was run for different load cases. Wave induced fatigue loads alone were first considered, then a diameter-independent fatigue load was introduced. It was concluded that, accounting for resonant waves only, the smaller the diameter of the support structure, the better.

# Acknowledgements

A very brief trace of my warm gratitude to some of the people who supported me during the process of writing this thesis. May our sharing have enriched both of us.

Thanks to my team of supervisors, for giving me a very valuable guidance when I was not capable of orientating myself. I learnt a lot from you all, on both a personal and professional level.

Pim, I honestly appreciate your human side; you know how much it counted to me.

Michael M., I will never forget bouldering with my Norwegian thesis supervisor: ”*In Norway, we believe that we are all equal...*”.

Michael A., thank you for believing in me since the start of this project, and for your guidance from the other side of the ocean. See you at Cape Canaveral, or Central Park.

Joris, I am really grateful to you for taking over my supervision at SGRE half way in the project. Great job on not ceding to the *fatigue* of explaining me the secrets of fatigue loads!

Thanks to everyone I had the honour to meet and talk to at SGRE. You played a big big role in making the office a great place to work, learn and laugh. Work hard, play (table football) hard. Thank you Col, for your great support, super vibes and spinning class.

Thanks to all the friends who I shared this bit of life with. Special mention to Marco, Kamil, Mario, Nunzia and Lino. Sometimes, happiness is real only when shared.

Thank you Giuli and Andre for supporting me in any possible way, and of course for giving me life. Thank you Giuli for teaching me that moments of crisis are pivotal moments in one person's life.

# Contents

**Summary** i

**Acknowledgements** ii

**List of Figures** viii

**List of Tables** xi

**Nomenclature** xiii

**1 Introduction** 1
- 1.1 Offshore Wind . . . . . 1
  - 1.1.1 Support Structures . . . . . 2
  - 1.1.2 OWT Design Process . . . . . 4
- 1.2 Problem Statement . . . . . 5
- 1.3 Literature Review . . . . . 5
- 1.4 Research Question . . . . . 6
- 1.5 Overview . . . . . 8

**2 Background** 9
- 2.1 Finite Element Method . . . . . 9
- 2.2 Modal Analysis . . . . . 12
- 2.3 Hydrodynamic Equations . . . . . 14
  - 2.3.1 Wave Kinematics . . . . . 14
  - 2.3.2 Wave Spectrum . . . . . 15
  - 2.3.3 Wave Loads . . . . . 15
- 2.4 Fatigue Damage . . . . . 17
  - 2.4.1 Time Domain . . . . . 20
  - 2.4.2 Frequency Domain . . . . . 21
  - 2.4.3 Wave Induced Fatigue Loads . . . . . 22

**3 Sensitivity Analysis** 25
- 3.1 Case Study . . . . . 25
  - 3.1.1 Support Structure . . . . . 26

3.1.2 Wave Climate . . . . . . . . . . . . . . . . . . . . . . . . . 27
3.2 Method . . . . . . . . . . . . . . . . . . . . . . . . . . . . . 28
3.3 Results and Discussion . . . . . . . . . . . . . . . . . . . . . . 31
3.3.1 Local Effects . . . . . . . . . . . . . . . . . . . . . . . . . 32
Sensitivity of the Natural Frequency-dependent Component . 33
Sensitivity of the Hydrodynamic Transfer Function . . . . . . 34
Sensitivity of the Structural Transfer Function . . . . . . . . . 37
3.3.2 Non-Local Effects . . . . . . . . . . . . . . . . . . . . . . . 38
3.3.3 Hypotheses Discussion . . . . . . . . . . . . . . . . . . . . 39
Averaged Sea-states . . . . . . . . . . . . . . . . . . . . . . 39
Parked Mode . . . . . . . . . . . . . . . . . . . . . . . . . 39
Soil Model . . . . . . . . . . . . . . . . . . . . . . . . . . 40
3.4 Conclusions . . . . . . . . . . . . . . . . . . . . . . . . . . . . 41

**4 Analytical Optimization** **43**
4.1 Method . . . . . . . . . . . . . . . . . . . . . . . . . . . . . 43
4.1.1 Case Study . . . . . . . . . . . . . . . . . . . . . . . . . . 44
4.1.2 Thickness . . . . . . . . . . . . . . . . . . . . . . . . . . . 46
4.1.3 Fatigue Load . . . . . . . . . . . . . . . . . . . . . . . . . 46
Wave Induced DEL . . . . . . . . . . . . . . . . . . . . . . 47
Diameter-independent DEL . . . . . . . . . . . . . . . . . . 52
4.1.4 Inputs . . . . . . . . . . . . . . . . . . . . . . . . . . . . 55
Diameter-independent DEL . . . . . . . . . . . . . . . . . . 55
Thickness Ratio . . . . . . . . . . . . . . . . . . . . . . . . 55
4.2 Results and Discussion . . . . . . . . . . . . . . . . . . . . . . 56
4.2.1 Wave Loads Only . . . . . . . . . . . . . . . . . . . . . . . 56
4.2.2 Waves and Wind Loads . . . . . . . . . . . . . . . . . . . . 58
4.2.3 Hypotheses Discussion . . . . . . . . . . . . . . . . . . . . 60
Thin Wall Assumption . . . . . . . . . . . . . . . . . . . . 60
Mass of RNA . . . . . . . . . . . . . . . . . . . . . . . . . 61
4.3 Conclusions . . . . . . . . . . . . . . . . . . . . . . . . . . . . 62

**5 Conclusion** **63**
5.1 Conclusions . . . . . . . . . . . . . . . . . . . . . . . . . . . . 63
5.1.1 Sensitivity Analysis . . . . . . . . . . . . . . . . . . . . . . 63
5.1.2 Analytical optimization . . . . . . . . . . . . . . . . . . . . 64
5.2 Recommendations . . . . . . . . . . . . . . . . . . . . . . . . . 65

**A Sensitivity Analysis** **67**

**B Analytical Optimization** **71**

**Bibliography** **73**

# List of Figures

1.1 Common types of support structures for bottom fixed and floating offshore wind turbines [8]. . . . . . . . . . . . . . . . . . . . . . . . 2
1.2 Overview of applied offshore wind support structure concepts until 2019 [26]. . . . . . . . . . . . . . . . . . . . . . . . . . . . . . . . . 3
1.3 Supports structure and its parts. . . . . . . . . . . . . . . . . . . . . . . . 3
1.4 Representation of current design process. . . . . . . . . . . . . . . . 4

2.1 Beam element, nodes, and DOF. . . . . . . . . . . . . . . . . . . . . . . 10
2.2 Annular cross section. . . . . . . . . . . . . . . . . . . . . . . . . . . . . 12
2.3 Waves frame of reference. . . . . . . . . . . . . . . . . . . . . . . . . . 15
2.4 Representation of wave forces on a cylindrical body [28]. . . . . . . 16
2.5 Single-sloped S-N curve. . . . . . . . . . . . . . . . . . . . . . . . . . . 19
2.6 Time domain method to estimate fatigue [22]. . . . . . . . . . . . . . 20
2.7 Dirlik's spectral method to estimate fatigue [22]. . . . . . . . . . . . 21

3.1 Representation of the case study. . . . . . . . . . . . . . . . . . . . . . 26
3.2 Sensitivity vs. diameter variation. . . . . . . . . . . . . . . . . . . . . . 28
3.3 Validation of the modeshape. . . . . . . . . . . . . . . . . . . . . . . . . 29
3.4 JONSWAP spectrum averaged according to Equation 3.1. . . . . . . . 30
3.5 Sensitivity of DEL to the diameter per elevation. . . . . . . . . . . . . 32
3.6 Sensitivity of DEL and its components at level $z$, due to a diameter variation at the same elevation. . . . . . . . . . . . . . . . . . . . . . . . 33
3.7 Local sensitivity of the function $f(\omega_0)$ and its components. . . . . . . 34
3.8 Local sensitivity of the hydrodynamic transfer function and its components. . . . . . . . . . . . . . . . . . . . . . . . . . . . . . . . . . . . . 35
3.9 Non-Local sensitivity of the modeshape, due to a diameter increases at three different levels. . . . . . . . . . . . . . . . . . . . . . . . . . . 36
3.10 Local sensitivity of the transfer function $H_{\mathrm{SH}}$ and its components. . . 37
3.11 Sensitivity surface of the structural transfer function. . . . . . . . . . 38
3.12 Representation of soil stiffness modeled with springs. . . . . . . . . . 41

4.1 Representation of the FE model of the MP. . . . . . . . . . . . . . . . 44
4.2 Relative percentage error of $A$ and $I$ due to the thin wall assumption. 45
4.3 Graphical representation of the continuous and discrete modeshape. 48

4.4 Example of spectrum of environmental loads of an offshore wind turbine [17]. . . . . . . . . . . . . . . . . . . . . . . . . . . . . . . . . . . . . 52
4.5 Representation of wave and wind loads combined, as shown in Equation 4.8. . . . . . . . . . . . . . . . . . . . . . . . . . . . . . . . . . . . 55
4.6 The thickness ratio as a function of $D$. . . . . . . . . . . . . . . . . . . 56
4.7 Mass and thickness vs. diameter for the case wave excitation only. . . 57
4.8 Spectral energy of the resonant wave vs. diameter. . . . . . . . . . . 57
4.9 Mass and thickness vs. diameter for the case of waves and wind excitation. . . . . . . . . . . . . . . . . . . . . . . . . . . . . . . . . . . 58
4.10 Mass vs. diameter (left) and first derivative(right) per load case. . . . 59
4.11 Line of the optima (left) and optimal diameter per load case (right). 60

A.1 Input diameter, thickness and element length distribution. . . . . . . 67
A.2 Comparison between the sensitivity of DEL computed with the original length distribution vs. the rediscretized one. . . . . . . . . . . . . 69
A.3 Distribution function of the waves. . . . . . . . . . . . . . . . . . . . . 70

# List of Tables

4.1 Optimal diameter and thickness for the load case considered. . . . . 58
4.2 Results of the optimization per load case. . . . . . . . . . . . . . . . . . 59

A.1 Input of the case study used in the sensitivity analysis. . . . . . . . . 67
A.2 Wave climate used for the sensitivity analysis. . . . . . . . . . . . . . 68

B.1 List of the inputs used in the analytical optimization. . . . . . . . . . 71

# Nomenclature

## Latin symbols

| | | |
|---|---|---|
| $A$ | Area | $\mathrm{m}^2$ |
| $a$ | S-N curve parameter | – |
| $b$ | Spectral moment | – |
| $D$ | Diameter | m |
| $d$ | Water depth | m |
| $E$ | Young modulus | Pa |
| $F$ | Fatigue damage | – |
| $f$ | Frequency | 1/s |
| $g$ | Gravity acceleration | $\mathrm{m/s}^2$ |
| $H$ | Transfer function | – |
| $h$ | Wave height | m |
| $I$ | Second moment of area | $\mathrm{m}^4$ |
| $i$ | Imaginary unit | – |
| $K$ | Stiffness | N/m |
| $k$ | Wave number | 1/m |
| $L$ | Element length | m |
| $M$ | Mass | Kg |
| $m$ | Wöhler exponent | – |
| $N$ | Number of cycles at failure | – |
| $n$ | Number of cycles | – |
| $a$ | Probability Density Distribution | – |

|  |  |  |
|---|---|---|
| $Q$ | External load | $N$ |
| $S$ | Power spectrum | $\mathrm{m}^2 \cdot \mathrm{s}$ |
| $T$ | Wave period | s |
| $t$ | Thickness | m |
| $v$ | Velocity of the wave particle | m/s |
| $x$ | In-plane horizontal coordinate | m |
| $y$ | Out-of-plane horizontal coordinate | m |
| $z$ | Vertical coordinate | m |

## Greek symbols

|  |  |  |
|---|---|---|
| $\Gamma$ | ”Gamma” function | – |
| $\gamma$ | Thickness ratio | – |
| $\tau$ | Spectral width parameter | – |
| $\Delta$ | Variation or range | – |
| $\eta$ | Wave distribution function | – |
| $\Theta$ | Peak-enhancement factor | – |
| $\lambda$ | Wave length | m |
| $\xi$ | Structural damping | – |
| $\rho$ | Material density | $\mathrm{kg/m}^3$ |
| $\sigma$ | Stress | Pa |
| $\Phi$ | Modeshape | – |
| $\phi$ | In-plane rotation | rad |
| $\omega$ | Angular frequency | rad/s |

## Subscripts

|  |  |
|---|---|
| A | Element A |

| | |
|---|---|
| B | Element B |
| $D$ | Drag component |
| DEL | Related to the DEL |
| $\mathrm{D} - \mathrm{ind}$ | Diameter-independent |
| eq | Equivalent |
| fix | Fixity depth |
| JS | JONSWAP |
| LT | Life Time (period) |
| $M$ | Inertia component |
| mid | Middle level |
| opt | Optimum |
| $p$ | Peak |
| PM | Pierson - Moskowitz |
| $S$ | Significant |
| $s$ | Solid |
| SB | Seabed |
| SH | to-selected-height |
| SL | Free surface line |
| t | Thickness-related |
| bot | Bottom level |
| $w$ | Water |
| $x$ | In-plane horizontal component |
| $y$ | Out-of-plane horizontal component |
| $z$ | Vertical component |

## Abbreviations

| | |
|---|---|
| 1P | Frequency of the Rotor |
| 3P | Blade Tower-Passing Frequency |
| DEL | Damage Equivalent Load |
| DOF | Degree Of Freedom |
| FE | Finite Element |
| HKZ | Hollandse Kust Zuid |
| JONSWAP | Joint North Sea Wave Project |
| OWT | Offshore Wind Turbine |
| PDF | Probability Density Function |
| PSD | Power Spectral Density |
| RNA | Rotor-Nacelle Assembly |
| SGRE | Siemens Gamesa Renewable Energy |
| S-N | Stress - Number of cycles |
| SWL | Still Water Level |
| TP | Transition Piece |

# Chapter 1

# Introduction

It is renowned that the human kind is dealing with one of the greatest challenges ever faced; stopping, and hopefully reversing the climate change, are goals that require everybody's effort. Among the aspects of our lives that need a radical change, the sources from which we generate energy are crucial ones; indeed, since the industrial revolution, the dramatic evolution in technology progressively increased the demand of energy supply, which was compensated by the exploitation of fossil fuels. A big downside of this worldwide exploitation protracted in time, is that the resulting waste gases have been contributing to global warming and consequently to climate change. For this reason, especially during the past decade, the transition to renewable energy has seen a strong boost, and so did offshore wind exploitation.

## 1.1 Offshore Wind

Apart from being greenhouse gases-free, offshore wind is a valid alternative because there is a big supply of wind in offshore sites. Moreover, compared to onshore wind, it is stronger and steadier because obstacles such as hills, mountains, forests and buildings are usually far from them. The remoteness of offshore sites also decreases the visual and auditory impacts of the wind turbines, allowing them to be bigger and more numerous, and thus to produce more power. In fact, the power produced by wind turbines scales with the second power of the rotor diameter.

Nevertheless, nothing comes for free. In fact, due to higher wind speeds and sea waves, the maritime environment requires complex infrastructures to transport, install and support the wind turbines, which lead to higher financial costs. According to T. Stehly et al. [25], one of the major contributors to the capital cost of an offshore wind power plant is the support structure of the wind turbines, ranging from $13\%$ to $29\%$ of the total cost, depending on the type of support structure adopted.

### 1.1.1 Support Structures

Several types of support structures exist, but the main distinction exists between *bottom founded* and *floating* support structures. Figure 1.1 shows the most common types of support structures, divided by bottom fixed and floating.

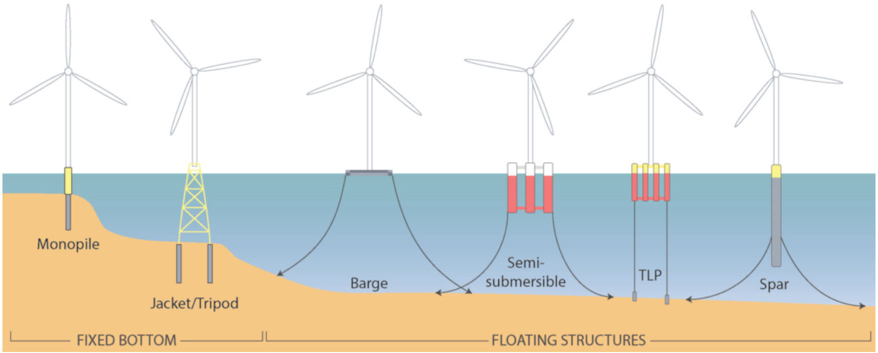

**Figure 1.1:** Common types of support structures for bottom fixed and floating offshore wind turbines [8].

The choice of the support structure is dictated by the water depth at the offshore site. Bottom founded are preferred for shallow to medium water depths of up to 60 m, after which they are expected to become economically unfeasible. Thus, floating structures offer a more convenient alternative for deep waters. Although the exploitation of offshore wind is starting to move toward deeper waters, bottom founded foundations, monopiles in particular, are nowadays the most used, as shown in Figure 1.2. This is mainly due to economic reasons, since bottom founded support structures are cheaper than floating ones, therefore shallow water sites have been mainly exploited so far; moreover, monopiles offer a simple and reliable solution based on decades of experience coming from designing, manufacturing and installing them.

Monopile-based support structures are composed of three main parts, the monopile, the transition piece (TP) and the tower, as shown in Figure 1.3. Each of these components is made of sub-elements. They can be seen as a group of ”cans” piled on top of each other, where each can is made of steel plates welded together. In the monopile and TP, the cans are connected through welds, whereas the tower has a more complex organization; this is usually due to the presence of multiple utilities inside it, such as stairs and platforms for the installation and maintenance crews,

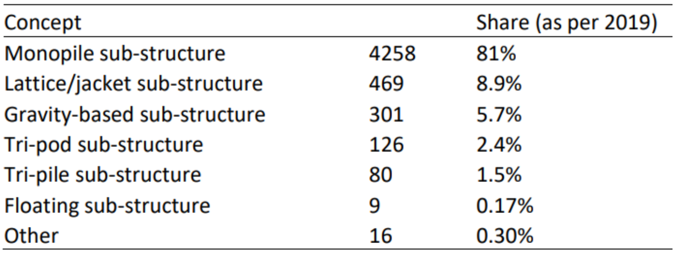

| Concept | | Share (as per 2019) |
|---|---|---|
| Monopile sub-structure | 4258 | 81% |
| Lattice/jacket sub-structure | 469 | 8.9% |
| Gravity-based sub-structure | 301 | 5.7% |
| Tri-pod sub-structure | 126 | 2.4% |
| Tri-pile sub-structure | 80 | 1.5% |
| Floating sub-structure | 9 | 0.17% |
| Other | 16 | 0.30% |

**Figure 1.2:** Overview of applied offshore wind support structure concepts until 2019 [26].

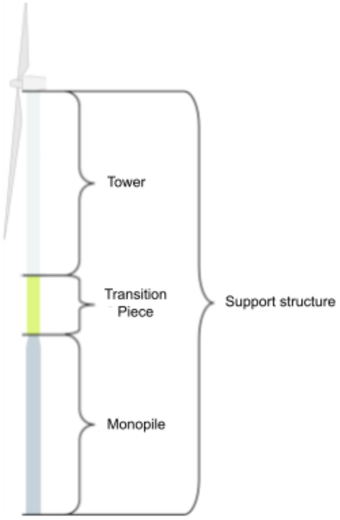

**Figure 1.3:** Supports structure and its parts.

and hosting structural damper at the top, but also for manufacturing procedures. Thus, each structural section is made of multiple cans piled on top of each other, that are usually bolted to the adjacent ones. Each section is then bolted to the others through flanges, that increase the tower's stiffness. The connections of the TP with the tower and the monopile are bolted; nevertheless, also grouted connections can be used.

### 1.1.2 OWT Design Process

Being the monopile-based support structures still widely adopted in offshore wind projects, an optimal design of these is of primary importance. The monopile and TP are designed by the foundation manufacturer, while the tower is designed by the wind turbine manufacturer. The optimal design of the monopile and TP, combined with the optimal design of the tower, possibly form an optimal design of the support structure. This process is characterized by some iterations between the foundation designer and the tower designer, who exchange information about loads and structural design, as shown in Figure 1.4. Although in theory an unlimited number of iterations could be needed for the designs to converge, typically the support structure design is concluded in 2-3 iterations.

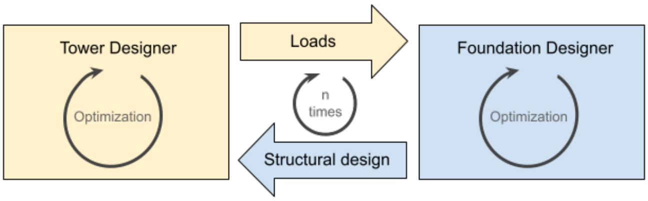

**Figure 1.4:** Representation of current design process.

Alternatively to this design approach, also integrated design exists, where the tower, TP and monopile are designed altogether. According to some studies [10] [11], this approach can lead to reduce significantly the structural mass and, if costs are hypothesized for simplicity to scale linearly with the structural mass, to cheaper support structures as well.

Four limit states are considered to design offshore wind support structures:

- **ULS** - Ultimate Limit State, caused by extreme waves and wind gusts acting on the structure.
- **FLS** - Fatigue Limit State, caused by cyclic loading exciting the structure.
- **ALS** - Accidental Limit State, in case of accidental events or failures.
- **SLS** - Serviceability Limit State, concerning the functionality of the structure under routine conditions.

Industrial experience suggests that the design is predominantly driven by FLS and ULS.

## 1.2 Problem Statement

Within the topic of structural optimization of offshore wind support structures, this thesis relates in particular to the fatigue driven design, in which waves excitation plays a major role. It is indeed important to understand what variables affect the wave induced fatigue loads more significantly, and how. This would help to increase the awareness of the designers, and allow them to include as many details as possible into the optimization process, useful to trim unnecessary costs and computational time. This type of analysis falls under the category of *sensitivity analysis*, that indeed aims to measure how sensitive a quantity is to its variables. The geometry of the system surely is one of the most important variables to account for, since it determines the response of the support structure to the external loads, and the final cost of the support structure, too.

## 1.3 Literature Review

With respect to the topic of *structural optimization of monopile-based support structures* and *sensitivity analysis of fatigue loads*, several researches have already been conducted. Here is a summary of the most relevant to this thesis:

- N. Maljaars [18] focused on the minimization of the support structure's mass using a Particle Swarm algorithm and an integrated approach, since many local optima were expected. The design variables used are the diameter and the wall thickness of the monopile-based support structure, and the constraints included fatigue loads, but also buckling and the support structure's maximum deflection. The optimization was run for several case studies, and it yielded a mass reduction of $13 - 17\%$.

- P. Markolefas [19] developed a fatigue analysis model of offshore wind turbine monopile-based support structures in the frequency domain, aiming to make the structural optimization more efficient. Fatigue loads are addressed in frequency domain with Dirlik's method, and a sensitivity analysis of the fatigue loads to the mesh chosen to model the structure is performed. The result is a reliable and quick model.

- L. Ziegler et al. [30] adopted a frequency domain method to perform the sensitivity analysis of fatigue, in particular to site conditions such as water depth, soil stiffness, wave height, and wave period. The Dirlik method is used to calculate fatigue damage in frequency domain, and it is found that: the method shows a >90% accuracy if compared to a time domain approach, and fatigue damage is especially sensitive to water depth and wave period. The method used is ideal for applications where fast simulations are needed.
- K.-H. Chew et al. [4] focused on analytical methods to calculate gradients of fatigue damage and equivalent fatigue loads, both in time and frequency domain, for implementation in the optimization of offshore wind turbine structures. Dirlik's method is applied to calculate fatigue in frequency domain, and the results are compared to finite difference differentiation. An interesting result of this work is that fatigue sensitivity analysis is very susceptible to the accuracy of response sensitivities, and this allows to propose several recommendations to help improving the overall quality of numerical sensitivities.
- K.-H. Chew et al. [5] conducted a relevant study that focused on an analytical gradient-based method to solve the problem of optimization of offshore wind turbine support structures efficiently. The constraints of the optimization include the fatigue load, whose sensitivity is evaluated analytically. It has been proved that analytical sensitivities are more accurate and efficient then the often used finite differences approximations.

## 1.4 Research Question

The extensive research conducted on the topic of structural optimization and sensitivity analysis of fatigue load gives an idea of the strong interest around them. The previous researchers gave important insights in these areas of interest, focusing on the accuracy and efficiency of the methods developed, rather than on the physical interpretation of the results. Ziegler performed sensitivity studies on fatigue to site conditions; nevertheless, there is not yet detailed research on *where* is beneficial to vary the support structure's geometry, and *why*. This thesis therefore aims to understand how the geometry of the support structure affects the wave induced fatigue loads. In the current structural design optimizations, the diameter distribution of the support structure is fixed per design run, whereas the wall thickness distribution undergoes the refining of the optimization. Thus, understanding how the diameter affects the fatigue loads, would benefit further the optimization of support structures. Hence, the main research question of the thesis is:

> *”How does varying the support structure’s diameter affect the wave induced fatigue loads of a monopile-based offshore wind turbine?”*

To tackle this research question, the following assignments were derived:

1. To determine the non-local effects on the wave induced fatigue load due to varying the support structure’s diameter.
2. To obtain the optimal support structure’s diameter that minimizes the mass of the support structure accounting for the fatigue constraint, following an analytical approach.

The first assignment aims to answer the research question through the sensitivity analysis of the wave induced fatigue loads in frequency domain. The sensitivity of the fatigue loads to a diameter variation applied at a certain elevation of the support structure, was obtained increasing by $5\%$ the diameter of the element at the height considered, and calculating the resulting variation of the fatigue loads at every elevation. The effect of the diameter variation was computed individually for each element of the support structure, i.e. when one element’s diameter is varied, the others remain unchanged. The variations of the fatigue loads evaluated at the same elevation where the diameter is varied, are named ”*local* effects”. On the other hand, the variations evaluated at those elevations where the diameter is not varied, are named ”*non-local* effects”. Thanks to this method, the non-local effects on the wave induced fatigue loads, due to the diameter variation applied to all elevations, were evaluated. Matlab was used to implement and run the analysis on a reference support structure and for a North-Sea wave climate, both provided by SGRE.

The second assignment was applied to a simplified support structure, in particular characterized by a diameter distribution constant along the height. A frequency domain approach was adopted to calculate the wave induced fatigue loads. The diameter that minimizes the support structure’s mass was calculated analytically, i.e. calculating the first derivative of the equation of mass as a function of the diameter constrained by the resistance to the fatigue damage, and finding its zeros. This method helped answering the research question by showing transparently what role is played by the diameter in the equations of the wave induced fatigue loads and support structure’s total mass. The analysis was performed by hand and with the aid of Wolfram Mathematica, for validation of the results and to produce insightful figures.

## 1.5 Overview

The report is divided into three main chapters. After the Introduction, Chapter 2 introduces the equations, formulas and concepts used to answer the research questions. Then, Chapter 3 starts by introducing the case study used to look for local and non-local effects of the diameter; then, the method adopted to calculate the sensitivity is explained and eventually the results obtained are shown and discussed. Chapter 4 explains the steps taken to perform the analytical optimization of the support structure's diameter, along with a discussion of the results obtained. Eventually, the lessons learnt throughout this work are wrapped up in the Conclusion chapter, followed by some recommendations for future research.

# Chapter 2

# Background

This chapter contains the basic knowledge that was used to conduct this work. Thus, a summary of the background theory, i.e. the mathematical tools and concepts on which this thesis was based, will be presented.

First, the theory used to describe the structure and its motion is described, going through the outlines of the Finite Element Analysis, and the modal analysis. Then, attention is given to the equations of the hydrodynamics: wave particles kinematics, wave spectrum and wave loads. Eventually, the computation of fatigue damage is introduced, both in time and frequency domain, focusing on the method used to calculate the wave induced fatigue loads in frequency domain.

## 2.1 Finite Element Method

To model the support structure, the finite element method was applied. It is used to give a discretized representation of a structure, using a mesh that allows for an efficient yet accurate enough representation of the continuum. Such method is suitable to analyze the vibrations of a structure, as it can be easily set up and run by calculators.

In this report, the support structure is divided into hollow cylindrical finite elements, which are modelled according to the *Euler-Bernoulli Beam Theory*. This theory is based on the following assumptions [13]:

- The material behaves accordingly to Hooke's law, i.e. it is linear elastic.
- Plane sections remain plane and perpendicular to the neutral axis.

Although the Euler-Bernoulli Beam Theory was chosen due to its simplicity, note that the *Timoshenko–Ehrenfest Beam Theory* shall be considered for a more accurate analysis of the structural motion. In fact, according to this theory the beam's sections are not bound to be perpendicular to the neutral axis, which has been proved to be more accurate to describe the shear behaviour of ”short” beams, i.e. beams whose length is small compared to the width (as for the elements of a monopile-based support structure). Every element has 2 nodes at its extremes, as represented in Figure 2.1.

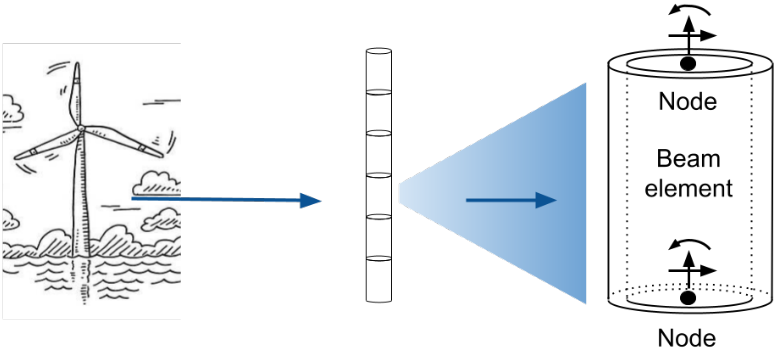

**Figure 2.1:** Beam element, nodes, and DOF.

Each node carries part the properties of mass and stiffness of a beam element; basically, the inertia and stiffness of the beam element are equally split into the two corresponding nodes. Since the structure is considered to lay into a 2-D plane, each node has three degrees of freedom: vertical and horizontal displacements, and in-plane rotation, as shown in Figure 2.1. What makes this method handy for the computation of vibrations, is that the stiffness and inertia properties of a structure can be gathered into matrix form. Therefore, a beam element would be represented by the following stiffness and mass matrices [9]:

$$\mathbf{K} = \begin{bmatrix} \frac{EA}{L} & 0 & 0 & -\frac{EA}{L} & 0 & 0 \\ 0 & \frac{12EI}{L^3} & \frac{6EI}{L^2} & 0 & -\frac{12EI}{L^3} & \frac{6EI}{L^2} \\ 0 & \frac{6EI}{L^2} & \frac{4EI}{L} & 0 & -\frac{6EI}{L^2} & \frac{2EI}{L} \\ -\frac{EA}{L} & 0 & 0 & \frac{EA}{L} & 0 & 0 \\ 0 & -\frac{12EI}{L^3} & -\frac{6EI}{L^2} & 0 & \frac{12EI}{L^3} & -\frac{6EI}{L^2} \\ 0 & \frac{6EI}{L^2} & \frac{2EI}{L} & 0 & -\frac{6EI}{L^2} & \frac{4EI}{L} \end{bmatrix} \tag{2.1}$$

$$\mathbf{M} = \frac{\rho_s \cdot A \cdot L}{420} \cdot \begin{bmatrix} 140 & 0 & 0 & 70 & 0 & 0 \\ 0 & 156 & 22L & 0 & 54 & -13L \\ 0 & 22L & 4L^2 & 0 & 13L & -3L^2 \\ 70 & 0 & 0 & 140 & 0 & 0 \\ 0 & 54 & 13L & 0 & 156 & -22L \\ 0 & -13L & -3L^2 & 0 & -22L & 4L^2 \end{bmatrix} \tag{2.2}$$

$E$, the Young modulus, and $\rho_s$, the volumetric mass, are properties of the beam's material; $A$ and $I$, are respectively the area and the second moment of area of the cross section at the considered node; $L$ is the length of the beam element. The matrices **M** and **K** in Equation 2.2 and 2.1 are oriented according to the following coordinates vector:

$$\mathbf{x}(t) = \begin{bmatrix} u_{z,1} \\ u_{x,1} \\ \phi_{y,1} \\ u_{z,2} \\ u_{x,2} \\ \phi_{y,2} \end{bmatrix} \tag{2.3}$$

Where $u_{z,j}$ is the vertical displacement of the $j$-th node, $u_{x,j}$ is the horizontal displacement and $\phi_{y,j}$ the in-plane rotation. the subscripts 1 and 2 represent respectively the bottom node and top node of one element.

For a beam element characterized by an annular cross section with external diameter $D$ and wall thickness $t$, as shown in Figure 2.2, the area and second moment of area are respectively:

$$A = \pi \cdot (D \cdot t - t^2) \tag{2.4}$$

$$I_{yy} = \frac{\pi}{64} \cdot (D^4 - (D - 2t)^4) \tag{2.5}$$

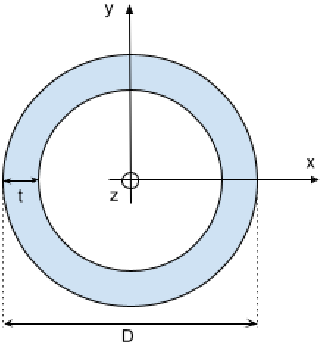

**Figure 2.2:** Annular cross section.

A relevant parameter often used to describe the geometry of the support structure's cross section is the ratio between its external diameter and the wall thickness, $D/t$. High values of $D/t$ indicate thinner sections, while low values indicate more bulky structures. As a rule of thumb, the $D/t$ ratio is in the order of 80 - 90. This rule of thumb is valid for diameters in the range of 4 to 8 m, because for larger diameter piles, very large wall thicknesses would result [26]. The limitations to this ratio come from buckling behaviour, but also from fabrication, transportation and installation. According to Steelwind Nordenham [21], $D/t$ ratios up to 160 would be feasible. Nowadays the average $D/t$ ratio of a support structure is around 140.

## 2.2 Modal Analysis

To describe the vibrations of structures, the modal analysis is used. The dynamics of a linear undamped system characterized by a mass and a stiffness matrix is described by the following equation of motion:

$$\mathbf{M} \cdot \ddot{\mathbf{x}}(t) + \mathbf{K} \cdot \mathbf{x}(t) = \mathbf{Q}(\mathbf{t}) \tag{2.6}$$

where $\mathbf{Q}(\mathbf{t})$ is a generic time-dependent load acting on the system. Please, note that for this section, the variable $t$ indicates the time, not the thickness. The modal quantities of such system are determined performing the modal analysis. These steps are followed:

1. The free vibrations of the system are considered, therefore the homogeneous form of Equation 2.6 is used. A solution of the type $\mathbf{x}(t) = \boldsymbol{\Phi} \cdot \exp(\lambda \cdot t)$ is chosen, where $\boldsymbol{\Phi}$ is the amplitude of the motion and $\lambda \in \mathbb{C}$ is a complex number [20]. Inputting this solution in the homogeneous form of Equation 2.6 yields:
$$\left(\lambda^2 \cdot \mathbf{M} + \mathbf{K}\right) \cdot \boldsymbol{\Phi} = \mathbf{0} \tag{2.7}$$

2. Equation 2.7 only have non zero solutions if the determinant of $\left(\lambda^2 \mathbf{M} + \mathbf{K}\right)$ determinant is zero. This condition yields the characteristic polynomial of the system:
$$\det\left(\lambda^2 \cdot \mathbf{M} + \mathbf{K}\right) = 0 \tag{2.8}$$
Solving the $r$ roots of Equation 2.8 yields the eigenvalues $\lambda_r$ of the system, where $r = 1 : N_{\mathrm{DOF}}$, where $N_{\mathrm{DOF}}$ is the number of degrees of freedom of the system. Thus, the natural frequencies can be derived, since for an undamped system the real part is zero [20]:
$$\lambda_+ = i \cdot \omega_r, \ \lambda_- = -i \cdot \omega_r \tag{2.9}$$
where $i = \sqrt{-1}$ is the imaginary unit.

3. Once the eigenvalues are determined, the system in Equation 2.7 can be solved for each mode to determine the corresponding modeshape $\boldsymbol{\Phi}_r$. It is important to consider that, since the matrix $\left(\lambda^2 \mathbf{M} + \mathbf{K}\right)$ is singular, the modeshape $\boldsymbol{\Phi}_r$ is not unique. In fact, any multiples of it satisfy the equation [14]. In this thesis, it was chosen to normalize the modeshape by its biggest element in absolute value.

4. Eventually, for the $r$-th mode, the modal mass $M_r$ and modal stiffness $K_r$ are determined using the following equations [14]:
$$M_r = \boldsymbol{\Phi}_{\mathbf{r}}{}^T \cdot \mathbf{M} \cdot \boldsymbol{\Phi}_{\mathbf{r}} \tag{2.10}$$

$$K_r = \mathbf{\Phi_r}^T \cdot \mathbf{K} \cdot \mathbf{\Phi_r} \tag{2.11}$$

The modal mass and stiffness are related through the following relation:

$$\omega_r^2 = \frac{K_r}{M_r} \tag{2.12}$$

The natural frequency $\omega_0$, the modeshape $\Phi_0$ and the modal stiffness $K_0$ of the first mode of vibration are needed as input for the wave induced fatigue load (see subsection 2.4.3).

## 2.3 Hydrodynamic Equations

The components needed to describe the hydrodynamic used in this thesis are:

- The kinematics of waves.
- The wave spectrum.
- The wave loads.

### 2.3.1 Wave Kinematics

The *linear wave theory* [15] is considered in this study. For such waves, the relation between the angular wave frequency, $\omega$, and the wave number, $k$, is given by the linear *dispersion relation* [15]:

$$\omega^2 = g \cdot k \cdot \tanh(k \cdot d) \tag{2.13}$$

where $g$ is the gravitational acceleration, and $d$ is the water depth.

For linear waves, the horizontal and vertical components of the wave particle velocity are determined respectively by [15]:

$$v_x = \frac{h \cdot \omega}{2} \cdot \frac{\cosh(k \cdot (z + d))}{\sinh(k \cdot d)} \cdot \sin(\omega \cdot t - k \cdot x) \tag{2.14}$$

$$v_z = \frac{h \cdot \omega}{2} \cdot \frac{\sinh(k \cdot (z + d))}{\sinh(k \cdot d)} \cdot \cos(\omega \cdot t - k \cdot x) \tag{2.15}$$

The frame of reference for the axes $x$ and $z$ is shown if Figure 2.3. Please note that in this section, the variable $t$ indicates the time, not the wall thickness.

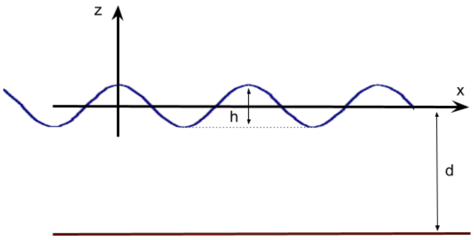

**Figure 2.3:** Waves frame of reference.

### 2.3.2 Wave Spectrum

Depending on the location-specific weather, different wave spectra may be needed. The spectra used in this thesis are Pierson-Moskowitz's and JONSWAP. The Pierson-Moskowitz spectrum is:

$$S_{\mathrm{PM}}(f) = 0.3125 \cdot h_{\mathrm{S}}^2 \cdot T_{\mathrm{p}} \cdot \left(\frac{f}{f_{\mathrm{p}}}\right)^{-5} \cdot \exp\left(-1.25 \cdot \left(\frac{f}{f_{\mathrm{p}}}\right)^{-4}\right) \tag{2.16}$$

where $h_S$ is the significant wave height, $T_p$ is the peak period, and $f_p$ is the peak frequency.

The JONSWAP spectrum can be viewed as the Pierson-Moskowitz spectrum multiplied by an additional factor, that is a function of the parameters $\Theta$ and $\tau$:

$$S_{\mathrm{JS}}(f) = S_{\mathrm{PM}}(f) \cdot (1 - 0.287 \cdot \ln \Theta) \cdot \Theta^{\exp\left(-0.5 \cdot \left(\frac{\frac{f}{f_p} - 1}{\tau}\right)^2\right)} \tag{2.17}$$

where $\tau$ is the spectral width parameter, which is equal to 0.07 if $f \leq f_p$, or 0.09 if $f > f_p$, and $\Theta$ is the peak-enhancement factor; it can be computed as a function of $h_S$ and $T_p$ [29], but it is common to use $\Theta = 3.3$.

### 2.3.3 Wave Loads

The renowned *Morison equation* is used to calculate the wave loads, because it is fast and relatively simple to implement. It expresses the force per unit length due the waves acting on a cylindrical body, as a linear superposition of an *inertia* component, proportional to the horizontal acceleration of the water particles relative to the structural acceleration, $\dot{v}_x(t) - \dot{u}_x(t)$, and a *drag* component, proportional to the square of the horizontal velocity of the water particles relatively to the velocity of the structure, $v_x(t) - u_x(t)$. Since monopiles support structures' acceleration and velocity are small compared to those of the water particles, they can be neglected; in this case, the absolute form of the Morison equation is:

$$Q_{\text{wave}} = Q_{\text{inertia}} + Q_{\text{drag}} =$$
$$= \frac{\pi}{4} \cdot \rho_w \cdot C_M \cdot D^2 \cdot \dot{v}_x(t) + \frac{1}{2} \cdot \rho_w \cdot C_D \cdot D \cdot v_x(t) \cdot |v_x(t)| \tag{2.18}$$

Here, $\rho_w$ is the water density, $C_M$ and $C_D$ are respectively the inertia and drag coefficients, $D$ is the outer diameter of the cross section of the cylinder. The dominant wave loads acting on a monopile are represented in Figure 2.4, as a function of the wave height $h$, monopile diameter $D$, and wave length $\lambda$. Since the Morison equation only describes the effects of drag and inertia loads, it is only valid for $\pi D/\lambda < 0.5$, which is often the case for offshore monopiles. Nevertheless, since

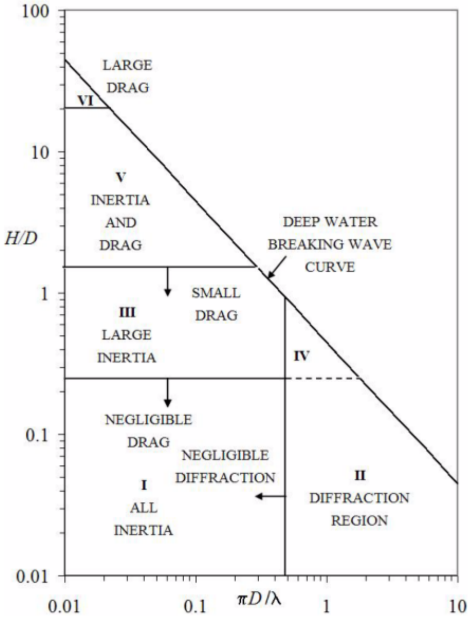

**Figure 2.4:** Representation of wave forces on a cylindrical body [28].

lately their size has been growing, it may be required to account for the diffraction effect. In this case, the inertia coefficient can be corrected to account for it. The diffraction correction can be performed based on the following formula [27]:

$$C_M = -2.5 \cdot \left(\frac{D(z)}{\lambda}\right)^3 + 7.53 \cdot \left(\frac{D(z)}{\lambda}\right)^2 - 7.9 \cdot \left(\frac{D(z)}{\lambda}\right) + 3.2 \leq 2 \tag{2.19}$$

Transforming Equation 2.18 in frequency domain yields the following hydrodynamic transfer function, that for the $r$-th mode of vibration returns:

$$\begin{aligned} H_{a,r}(\omega) = \omega \cdot \int_{z_{\mathrm{SL}}}^{z_{\mathrm{SB}}} c_h(\hat{z}) \cdot \eta(\hat{z}, \omega) \cdot \Phi_r(\hat{z}) \cdot d\hat{z} \, + \qquad (2.20) \\ + \, i \cdot \rho_w \cdot \omega^2 \cdot \int_{z_{\mathrm{SL}}}^{z_{\mathrm{SB}}} C_M(\hat{z}) \cdot \frac{\pi \cdot D(\hat{z})^2}{4} \cdot \eta(\hat{z}, \omega) \cdot \Phi_r(\hat{z}) \cdot d\hat{z} \end{aligned}$$

where $c_h$ is the hydrodynamic damping coefficient, which accounts for both the drag coefficient $C_D$ and the linearization of the wave particle velocity, and the *distribution function* of the horizontal velocity field, $\eta(z, \omega)$, is:

$$\eta(z, \omega) = \frac{\cosh\Big(k \cdot (z + d)\Big)}{\sinh\left(k \cdot d\right)} \tag{2.21}$$

where $z$ is the vertical coordinate with origin at the SWL. More details on Equation 2.20 can be found in Hapel, Chapter 4.4 [12]. The effect of stretching wave kinematics to the wave crest is neglected in frequency domain, due to its inherent non-linearity.

## 2.4 Fatigue Damage

A structure experiences fatigue damage when it is excited by cyclic loads. Due to this, the structure oscillates and develops stresses that allow cracks to form and/or propagate within the material, which may eventually cause it to fail. The speed of propagation depends on the response of the structure to the external loads. Not having control on the environment, the geometry of the structure is the key for a good design, as it determines its eigenvalues, hence how wide and how often the structure vibrates in response to external loads. In fact, a structure whose natural frequencies fall around the peaks of the environmental loads' spectrum is likely to have a shorter life span, compared to a structure whose natural frequencies are far from such peaks. Therefore, a structure that is not properly designed to endure fatigue damage, might experience a failure during its operative life, something that has to be seriously prevented.

Mathematically, as it is recommended in DNV-OS-J101 [29], under the assumption of linearly cumulative damage, the fatigue damage $F$ can be seen as the summation over the stress ranges that the structure experiences during an period of time, of the ratios between the number of cycles experienced at one stress range, $n_i$, and the number of cycles that the structure can stand before failure at the same stress range, $N(\Delta\sigma_i)$. It is therefore handy to calculate a constant-amplitude *equivalent stress range*, $\Delta\sigma_{\text{eq}}$, that yields the same fatigue damage as all the stress ranges, for a fixed equivalent number of cycles, $n_{\text{eq}}$. This is described by the Palmgren-Miner rule, according to which, the fatigue damage is [29]:

$$F = \sum_{i=1}^{m} \frac{n_i}{N(\Delta\sigma_i)} = \frac{n_{\text{eq}}}{N(\Delta\sigma_{\text{eq}})} \tag{2.22}$$

where the equivalent number of cycle is usually $n_{\text{eq}} = 10^7$ [7]. Thus, the fatigue damage $F$ is the ratio of the accumulated damage divided by the total damage that a structure can take before failure, that happens for $F = 1$.

During the past century, the behavior to fatigue of several materials has been tested, tracking the stress ranges and number of cycles at failure. These results have been then gathered in the so-called S-N curves, i.e. logarithmic plots that describes how many cycles $N$ a structure can resist before failure due to the stress range $\Delta\sigma$. Such plots are described by the following equation:

$$\log(N) = \log(a) - m \cdot \log(\Delta\sigma) \text{ [7]}, \quad \text{or} \quad N = \frac{a}{\Delta\sigma^m} \tag{2.23}$$

where $\log(a)$ is the intercept of the mean S-N curve with the $\log(N)$ axis, and $m$ is the negative inverse slope of the S-N curve (see Figure 2.5). There are different values of $\log(a)$ and $m$, per material. Moreover, the S-N curves are in general bi-linear, therefore, per material, there are usually two different pairs of $a$ and $m$, depending on the number of cycles considered. Nevertheless, in this thesis single-sloped S-N curves will be considered, as they are more handy to perform analytical calculations.

To calculate the stress due to the bending moment $M_{yy}$ around the $y$ axis (Fig-

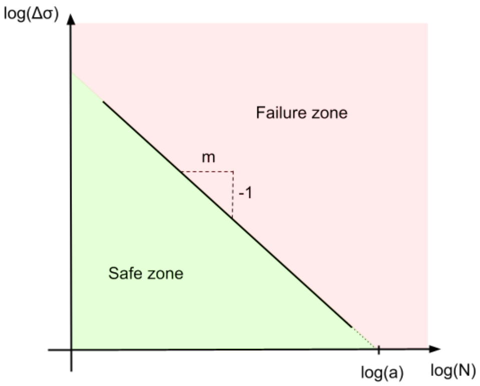

**Figure 2.5:** Single-sloped S-N curve.

ure 2.2), this equation is used:

$$\Delta\sigma = \frac{M_{yy} \cdot D/2}{I_{yy}} \tag{2.24}$$

where $D/2$ is the distance between the outer diameter of the cross section of the support structure and the neutral axis, and $I_{yy}$ is the second moment of area of the section perpendicular to the neutral axis, with respect to the $y$ axis.

When the equivalent stress $\Delta\sigma$ is considered, Equation 2.24 becomes:

$$\Delta\sigma_{\text{eq}} = \frac{\text{DEL} \cdot D/2}{I_{yy}} \tag{2.25}$$

where DEL is the damage equivalent load, thus the constant-amplitude equivalent bending moment that induces an equivalent stress range that in $n_{\text{eq}}$ cycles causes the same damage as all the stress ranges present in the considered load history.

Inserting Equation 2.25 in Equation 2.23, and this into Equation 2.22, gives the fatigue damage due to the DEL:

$$F = \frac{n_{\text{eq}} \cdot (\Delta\sigma_{\text{eq}})^m}{a} \tag{2.26}$$

The fatigue damage accumulated throughout a certain period of time can be scaled to a desired time interval, according to the following formula:

$$F_{\text{new}} = F_{\text{old}} \cdot \frac{T_{\text{new}}}{T_{\text{old}}} \tag{2.27}$$

Where $T_{\text{new}}$ is the desired time period, and $T_{\text{old}}$ is the time period considered for the previous damage.

To determine the number of cycles $n_i$ per stress range $\Delta\sigma_i$, different methods exist in time domain and frequency domain; they will be described in the next paragraphs.

### 2.4.1 Time Domain

Following the time domain approach, the time series of a cyclic stress range is decomposed using the Rainflow Algorithm into individual stress cycles, and the number of occurrences of each of them is calculated. Here, the assumption is made that the individual cycles may be superimposed upon one another. (For the complete description of the Rainflow Counting algorithm, please see [2].) The stress ranges and their respective numbers of cycles are then used in the Palmgren-Miner rule, which allows to calculate the fatigue damage. The steps to calculate the fatigue damage in time domain are summarized in Figure 2.6.

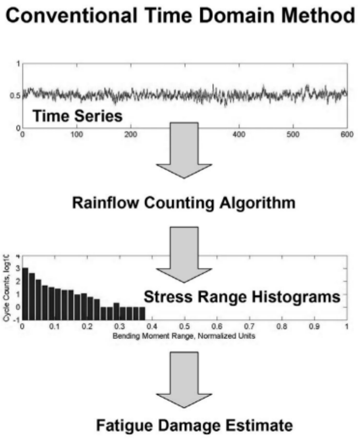
Conventional Time Domain Method
1
0.5
0
Time Series
0
100
200
400
500
600
Rainflow Counting Algorithm
Cycle Counts, log10
4
3
2
1
0
-1
Stress Range Histograms
0
0.1
0.2
0.3
0.4
0.5
0.6
0.7
0.8
0.9
1
Bending Moment Range, Normalized Units
Fatigue Damage Estimate

**Figure 2.6:** Time domain method to estimate fatigue [22].

Nevertheless, for preliminary structural design the time domain approach may result too expensive computationally. Spectral methods offer instead a more agile solution.

### 2.4.2 Frequency Domain

Different methods exist to estimate the fatigue damage in frequency domain, yet the most reliable and widely used for structural design is Dirlik's method [24]. In general, the frequency domain approaches consist of estimating the probability density distribution $p_R$ of the stress ranges from their power spectrum $S(f)$, and then calculate the fatigue damage with an "integral version" of the Miner's sum:

$$F = \frac{E[P]}{a} \cdot \int_0^{\infty} (\Delta\sigma)^m \cdot p_R \cdot d\Delta\sigma \quad [24] \tag{2.28}$$

where $E[P]$ is the expected number of peaks per unit time.

Dirlik proposed a method to estimate a stress range PDF that may be applied to both wide and narrow-band Gaussian processes. This method was developed by considering more than 60 different processes with power spectra of various shapes, computing their stress range PDF in the time domain via Rainflow counting and fitting a general expression for the stress range PDF in terms of the 0th, 1st, 2nd, and 4th spectral moments. Figure 2.7 summarizes the steps of Dirlik's spectral method. This description of Dirlik's method [6] is based on P. Ragan et al. [22].

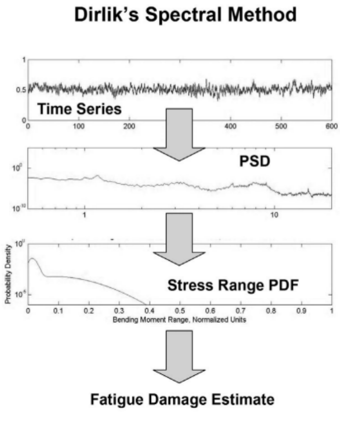

**Figure 2.7:** Dirlik's spectral method to estimate fatigue [22].

The main advantage of using frequency domain methods to compute the fatigue damage is to avoid the computationally expensive steps due to simulations and Rainflow Counting. In fact, time domain methods require usually many simulations to:

1. Account for the larger stress cycles that rarely occur and are very important to the fatigue damage experienced by the structure.
2. Achieve an adequate resolution of the stress range histograms needed for the Rainflow algorithm.

Dirlik's method, instead, requires less computational effort to obtain the loads power spectrum with less statistical uncertainty; this is then used to estimate the stress range PDF.

Dirlik's method works for both wide and narrow-band Gaussian processes. In this thesis, the assumption of narrow-band spectrum is taken, because the support structure has a low structural damping and there is not aerodynamic damping, as the wind turbine is assumed in parked mode. As explained in Barltrop [3], the PDF of the peaks of a narrow-band process follows a Rayleigh distribution, and so does the PDF of the stress range. In this case, the DEL is calculated according to the following equation:

$$\mathrm{DEL} = (8 \cdot b_0)^{\frac{1}{2}} \cdot \left[\Gamma\left(\frac{2+m}{2}\right)\right]^{\frac{1}{m}} \tag{2.29}$$

where $b_0$ is the 0th spectral moment of the bending moment power spectrum.

### 2.4.3 Wave Induced Fatigue Loads

Based on the formulation given by Seidel [23], Equation 2.29 is then used to determine the wave induced fatigue loads on the low-damped support structure of a parked wind turbine. The 0th spectral moment of the power spectrum is the variance of the spectrum. Therefore, assuming a constant slope of the S-N curve $m = 4$, the DEL for $n_{\mathrm{ref}}$ number of cycles results:

$$\mathrm{DEL} = 2^{\frac{3}{2}} \cdot \sigma_M \cdot \left[\Gamma\left(\frac{2+4}{2}\right)\right]^{\frac{1}{4}} = 3.363 \cdot \sigma_M \tag{2.30}$$

where $\sigma_M$ is calculated as done by Seidel [23]:

$$\sigma_M = \sigma_M(z) = \sigma_{u,\mathrm{RNA}} \cdot H_{\mathrm{SH}}(z) \tag{2.31}$$

$\sigma_{u,\mathrm{RNA}}$ is the standard deviation of the tower displacement at tower top, and $H_{SH}(z)$ is the structural transfer function, that allows calculate the standard deviation of the bending moment at any elevation $z$:

$$H_{SH}(z) = \omega_0^2 \cdot \int_z^{z_{\mathrm{RNA}}} \Phi_0(\hat{z}) \cdot \mu(\hat{z}) \cdot (\hat{z} - z) \cdot d\hat{z} \tag{2.32}$$

This transfer function accounts for the inertial loads due to the acceleration of the elements above the elevation at which the transfer function is calculated. Note that only the first mode of vibration is considered because it is close to the peak of the wave spectrum, whereas the others are further away and thus do not give a significant contribution to the structure's motion.

The standard deviation squared of the displacement at tower top is:

$$\sigma_{u,\mathrm{RNA}}^2 = \Phi_0(z_{\mathrm{RNA}})^2 \cdot H_{a,0}^2 \cdot S_{\zeta\zeta}(\omega_0) \cdot \int_{-\infty}^{\infty} |H_0(\omega)| \cdot d\omega \tag{2.33}$$

where $\Phi_0(z_{\mathrm{RNA}}) = 1$, because of the normalization of the modeshape, $H_{a,0}$ is the hydrodynamic transfer function, $S_{\zeta\zeta}(\omega_0)$ is the wave energy spectrum evaluated at the first angular natural frequency, and $H_0(\omega)$ is the dynamic transfer function of a linear system. The solution of the integral in Equation 2.33 is computed analytically as done by Seidel [23]:

$$\int_{-\infty}^{\infty} |H_0(\omega)| \cdot d\omega = \frac{\pi}{K_0^2 \cdot 4\xi_0} \cdot \omega_0 \tag{2.34}$$

where $\xi_0$ is the structural damping of the first mode. This term accounts for the stiffness of the structure, the structural damping, and the number of cycles, that is represented by the natural frequency of the structure.

It is assumed that the drag term is negligible, since it is small for fatigue waves [16]; this assumption is valid for typical monopile diameters for fatigue wave conditions encountered in the North or Baltic Sea. Therefore, the hydrodynamic transfer function (Equation 2.20) at the first natural frequency results:

$$H_{a,0} = \rho \cdot \omega_0^2 \cdot \int_{z_{\mathrm{SB}}}^{z_{\mathrm{SL}}} C_M(\hat{z}) \cdot \frac{\pi \cdot D(\hat{z})^2}{4} \cdot \eta_0(\hat{z}) \cdot \Phi_0(\hat{z}) \cdot d\hat{z} \tag{2.35}$$

The DEL calculated as in Equation 2.30 is the damage equivalent load for the number of cycles $n_{\mathrm{ref}}$, which is computed as:

$$n_{\mathrm{ref}} = f_0 \cdot T \tag{2.36}$$

Usually the 1-Hz equivalent DEL is used, where the number of reference cycles $n_{\mathrm{ref,1Hz}}$ is the number of seconds within the interval T, i.e.:

$$n_{\mathrm{ref,1Hz}} = f_{\mathrm{ref,1Hz}} \cdot T = T \tag{2.37}$$

The conversion to 1-Hz equivalent yields:

$$\mathrm{DEL} = 3.363 \cdot \sigma_M \cdot \left(\frac{n_{\mathrm{ref}}}{n_{\mathrm{ref,1Hz}}}\right)^{\frac{1}{m}} = 3.363 \cdot \sigma_M \cdot f_0^{\frac{1}{4}} \tag{2.38}$$

Therefore, the resulting equation of the 1-Hz damage equivalent load is:

$$\mathrm{DEL}_{\mathrm{wave}}(z) = \mathrm{DEL}(z) = 1.8825 \cdot \sqrt{S_{\zeta\zeta}(\omega_0)} \cdot \frac{1}{K_0} \cdot \sqrt{\frac{1}{\xi_0}} \cdot \omega_0^{\frac{3}{4}} \cdot H_{a,0} \cdot H_{\mathrm{SH}}(z) \tag{2.39}$$

The 1-Hz equivalent DEL is independent of the intended service life, therefore, combined with the number of seconds during the intended service life, it yields the total damage. Equation 2.39 later on is referred to in the following form:

$$\mathrm{DEL}(z) = f(\omega_0) \cdot H_{a,0} \cdot H_{\mathrm{SH}}(z) \tag{2.40}$$

where $f(\omega_0)$ gathers those components that are related to the natural frequency:

$$f(\omega_0) = 1.8825 \cdot \sqrt{S_{\zeta\zeta}(\omega_0)} \cdot \frac{1}{K_0} \cdot \sqrt{\frac{1}{\xi_0}} \cdot \omega_0^{\frac{3}{4}} \tag{2.41}$$

# Chapter 3

# Sensitivity Analysis

As the name suggests, the sensitivity analysis is a study that measures how *sensitive* a certain quantity is to the parameters on which it depends, explicitly and/or implicitly. There are several ways to perform it. An important distinction exists between ”local” and ”global” sensitivity analyses. For the scope of this thesis, a ”local” sensitivity analysis is used. This type of analysis applies small changes to the parameters considered, to capture how the result changes; this is equivalent to the concept of derivative, i.e. a linearization of the expected change due to the small change of some parameters. The ”global” sensitivity analysis, on the other hand, differs from the first one because it attempts to understand changes in the results due to large changes in the parameters.

This chapter discusses the methodology developed to perform the ”local” sensitivity analysis of the wave induced fatigue loads, in frequency domain, acting on a support structure supporting an offshore wind turbine, with respect to its diameter; such methodology is then applied to a case study. First, an outline of the case study is given, followed by the method used to calculate the sensitivity of the fatigue loads. Then, the results of the sensitivity analysis applied to the case study considered are shown, along with a description and interpretation of what is observed. Eventually some of the most relevant hypotheses are discussed, to speculate on how they have affected the results.

## 3.1 Case Study

The case study considered in this chapter refers to a monopile supporting an offshore wind turbine in parked mode; i.e. the monopile is excited by waves in absence of relevant wind loads. This mode mainly occurs during the downtime condition, i.e. when the wind turbine is not operating because of off-nominal environmental conditions, major failures and catastrophic events. Although the shorter the downtime the better, the parked mode cannot be neglected, as nowadays the typical design assumption for this condition is $\sim 2.5$ years.

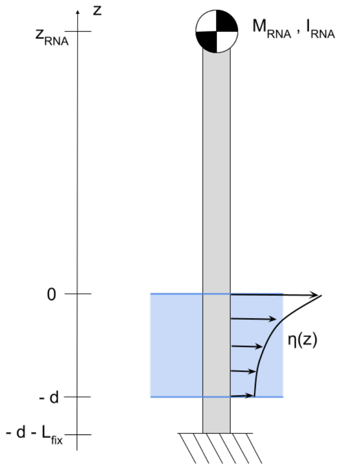

**Figure 3.1:** Representation of the case study.

The hub height is $z_{\text{RNA}} = 150.0$ m, The water depth is $d = 50.0$ m, and the distance from the mudline to the fixity level is 22.0 m. Thus, the total length of the structure is 222.0 m.

### 3.1.1 Support Structure

The geometry and the properties of the support structure were provided by SGRE. In particular, the following parameters:

- External diameter distribution, $D(z)$;
- Thickness distribution, $t(z)$;
- Length of the sub-elements, $L(z)$;
- Steel properties: density $\rho_s$, Young's modulus $E$, shear modulus $G$;
- Mass and mass moment of inertia of the RNA, respectively $M_{\text{RNA}}$ and $I_{\text{RNA}}$;

See Figure A.1 and Table A.1 in Appendix A for the summary of the inputs used.

Figure 3.1 shows a representation of the case study.

In this case study, the type of connections between plates and cans were simplified. The monopile was modeled as a whole hollow cylindrical structure, whose diameter and thickness vary discontinuously along its length, following the geometry of the structure provided by SGRE. Moreover, the marine growth, appurtenances and corrosion effects that act on the monopile and transition piece were neglected; in general, the first two elements cause an increase to the wave loads and the total mass of the structure, and so affect its dynamics; the latter, impacts the lifetime and the stability of the structure, as an oxidized structure is more prone to failures. Although important for a detailed structural design, these effects were neglected for simplicity, because the marine growth and appurtenances contributions are low relatively to the total wave loads and structural mass, and because anti-corrosion measures prevent the structure from experiencing critical damages.

The soil stiffness was also modeled simply, adopting a fixity depth model, i.e. the monopile is considered clamped at a *fixity depth* below mudline. Accounting for such length yields a rough approximation of the soil stiffness. The fixity depth is usually chosen as 3-5 times the monopile's diameter, nevertheless here it was considered diameter-independent, because the variation applied to the diameter is local, as it will be explained in section 3.2; thus, it is reasonable to keep the fixity depth unvaried.

### 3.1.2 Wave Climate

In parked mode, the wave climate is the most important environmental factor to account for. In general, it is described by different sea states, each of which is characterized by a significant wave height $H_S$, a peak period $T_p$, and a probability of occurrence $p$. Usually based on a combination of ”hindcast models” and on-site measurements, these data provide information about how often waves with a determined height and frequency are expected to hit a structure, throughout its lifetime.

For this case study, a North Sea wave climate was provided by SGRE's hydrodynamics team. A polynomial fit was done on the data-set for $H_s$, and for $T_p$, from the hindcast statistics time series from Hollandse Kust Zuid (HKZ) [1], defining one sea state per wind speed, up to 32 m/s.

It is important to remark that HKZ is a shallow site, therefore it does not perfectly represent a North Sea site of 50 m depth, as in general deeper waters are correlated with rougher sea states for the structure. Nevertheless, this is partly balanced by the conservative assumption of considering waves coming from the same direction.

One last remark, is that the lumping method used to represent the full data-set is quite rough, i.e. industry standard are not respected; on the other hand, the discrepancies due to this are smaller, compared to those caused by the assumptions presented above. The wave inputs are gathered in Appendix A, Table A.2.

## 3.2 Method

As mentioned in the introduction to this chapter, calculating the "local" sensitivity of the DEL with respect to the diameter, is basically equivalent to compute the derivative $d\,\mathrm{DEL}/d\,D$. To do so, an analytical method was firstly attempted; nevertheless, the analytical formulas of some relevant components of the wave-induced DEL, such as the modal quantities, contained complexities that did not allow to proceed as planned. Therefore, a finite difference approach was used, varying one element's diameter alone per time by a certain amount, and comparing the resulting DEL$(z)$ to the one of the unvaried structure. The variation was set to $+5\%$ of the element's diameter, since in absolute terms it translates to increases in the range of 25.0 - 58.0 cm, that is a magnitude relatable to reality.

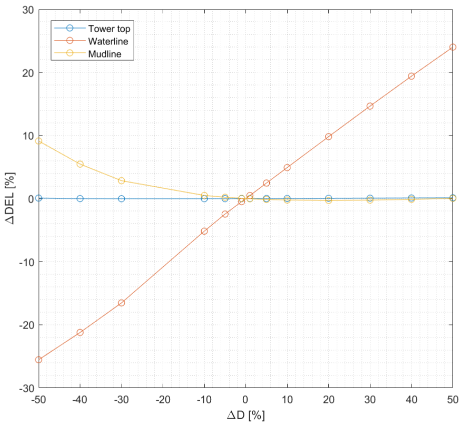

**Figure 3.2:** Sensitivity vs. diameter variation.

Moreover, it was observed that the derivatives obtained have a quite linear behavior, since very similar results were obtained calculating the derivatives for different variation percentages, from -50% to +50%, as shown in Figure 3.2. As it can be observed, around tower top and waterline the sensitivities are reasonably linear for any variations, while around mudline it is not linear for positive and negative variations greater than $10\%$.

Matlab was used to implement and run the calculations. The DEL was first calculated at each node of the reference structure presented in section 3.1. The steps needed to calculate the DEL in frequency domain, according to Equation 2.39, are the following:

- The modal analysis, as described in section 2.2; this was needed to calculate the natural frequency, the modeshape, and the modal stiffness of the first mode of vibration of the fore-aft motion. For this analysis, a FE model was set up, as described in section 2.1, where each node has 2 DOFs: in-plane horizontal displacement, and in-plane rotation. Therefore, the shear and bending stiffness were accounted for, while the geometric stiffness, due to the axial loads given by the RNA mass and the structure mass, was not. The FE model was implemented from scratch, and it was validated against a reference provided by SGRE. The natural frequency overestimated SGRE's by $3\%$, while the maximum deviation of the modeshape underestimated SGRE's by $2.5\%$. Therefore, the structure showed a slightly stiffer behaviour, compared to the reference.

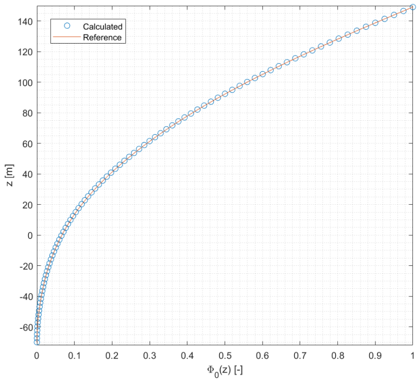

**Figure 3.3:** Validation of the modeshape.

Figure 3.3 shows the validation of the modeshape against SGRE's. Note that the for simplicity, the following approximation was applied: the modal quantities were determined for an undamped system, whereas Seidel's approach accounts for structural damping (see Equation 2.34).

- The structural transfer function $H_{\mathrm{SH}}$ described in Equation 2.32;
- The hydrodynamic transfer function $H_{a,0}$ described in Equation 2.35;
- The wave spectral energy evaluated at the first natural frequency $S_{\zeta\zeta}(\omega_0)$; the JONSWAP spectrum was chosen to represent the wave energy spectrum (Equation 2.17). Since each sea-state yields a different wave spectrum, and the DEL is proportional to $\sqrt{S_{\zeta\zeta}(\omega_0)}$, an averaging was applied to calculate the DEL that best represents the whole wave climate. Thus, the sea-states were averaged as follows:

$$\left[\sqrt{S_{\zeta\zeta}(\omega_0)}\right]_{\mathrm{avg}} = \left(\sum_j (S_{\zeta\zeta,j}(\omega_0))^{\frac{m}{2}} \cdot \hat{p}_j\right)^{\frac{1}{m}} \tag{3.1}$$

where $\hat{p}_j$ is the probability of occurrence of the j-th sea-state, normalized by

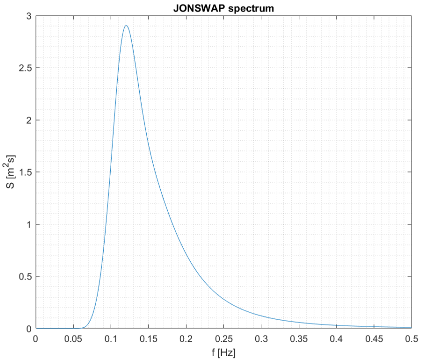

**Figure 3.4:** JONSWAP spectrum averaged according to Equation 3.1.

the sum of the sea-states' probability of occurrence. The averaged spectrum is plotted in Figure 3.4. Note that the natural frequency of the structure considered is on the right side of the peak, according to the usual design values of $\omega_0$.

Thus, the DEL is calculated at each node. Consequently, the damage equivalent load is computed for a $5\%$ increase of the diameter of element $i$. The sensitivities are obtained calculating the relative percentage variation between $\mathrm{DEL}_i(z)$ and $\mathrm{DEL}_0(z)$, as follows:

$$\Delta\,\mathrm{DEL}_i(z) = \frac{\mathrm{DEL}_i(z) - \mathrm{DEL}_0(z)}{\mathrm{DEL}_0(z)} \cdot 100 \tag{3.2}$$

To understand the role played by each of the DEL's components, the total sensitivity was decomposed into its parts.

During the analysis of the results, it was noticed that in correspondence of the flanges, whose vertical length is much smaller than the other elements, the sensitivity of DEL had a significant drop. Thus, it was deduced that the element's length affects the sensitivity of the DEL due to diameter variations, because varying the diameter of a shorter element has a lower impact on the DEL, compared to a change performed on a longer element. Filtering out this effect could not be simply done by normalizing the results by the elements' lengths, since it was observed that it flipped the drops into peaks. What was done instead, was to rediscretize the elements' length distribution, into a homogeneous one, i.e. of equally long elements; the same number of elements, and distribution of diameter and thickness were kept. This approach allowed to obtain results clean from the influence of the relative difference between elements length, although it was noticed that the overall behavior of the sensitivity remained rather similar. The comparison between the two cases is shown in Appendix A, Figure A.2.

## 3.3 Results and Discussion

Applying this method to the case study introduced earlier, yielded the results of the sensitivity analysis of the DEL to the structure's diameter. A graphical representation gives a direct overview of the sensitivity behavior. Hence, the results can be observed in the figures presented in the following pages. In the following 3-D plots, the axis named "*Variation Coordinate*" indicates where the diameter was increased by $5\%$; the "*Evaluation Coordinate*" indicates the elevation where the DEL was calculated.

The surface plotted in Figure 3.5 shows the effects of a diameter increase performed at every element of the structure, on the wave induced DEL($z$). According to this plot, the diameter has a low impact on the DEL above the waterline, since $\Delta\mathrm{DEL} \to 0\%$, whereas it has a greater impact below the waterline, resulting in variations in DEL within the range of -2.5$\%$ and $4\%$. Moreover, it shows that applying

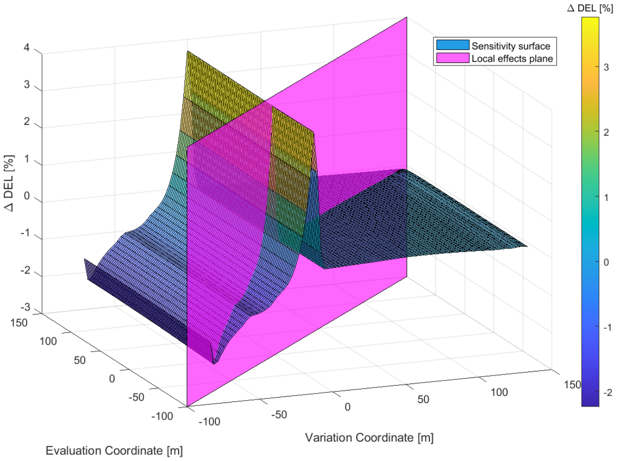

**Figure 3.5:** Sensitivity of DEL to the diameter per elevation.

a diameter variation along the Variation Coordinate, the DEL variation is quite constant along the Evaluation Coordinate. Therefore, it can be stated that, according to the approach followed, non-local effects are observed, although they are basically equal to the local ones.

In light of these two main considerations, an interpretation of the local effects is first given; then, it will be explained why the non-local effects do not differ significantly from the local ones.

### 3.3.1 Local Effects

Figure 3.6 shows the percentage variation of the wave induced DEL, evaluated at the same elevations where the elements' diameter is increased by $5\%$. Basically, it is the curve that results from intersecting the sensitivity surface with the vertical plane passing through the horizontal diagonal from $[-100,\,-100]$ m to $[150,\,150]$ m, as shown in Figure 3.5. It shows clearly the trend of the DEL sensitivity: it is close to zero along the tower, then increases to a positive peak right below the waterline, after which starts decreasing and becomes negative for water depths $> 16$ m.

To better understand what causes the trend observed in Figure 3.6, the different components of Equation 2.40, $f(\omega_0)$, $H_{a,0}$, and $H_{SH}$, were plotted in the same fig-

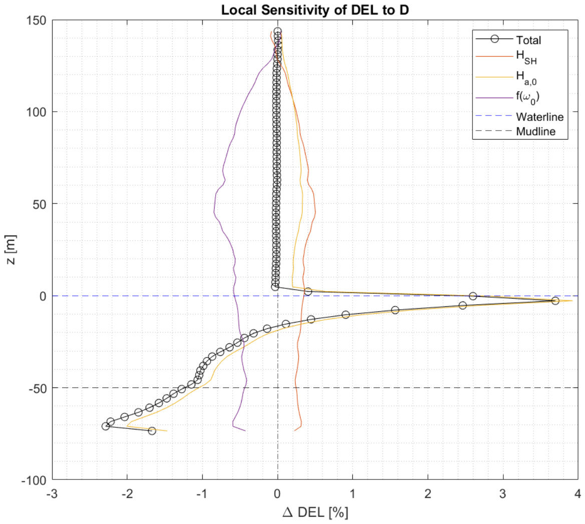

**Figure 3.6:** Sensitivity of DEL and its components at level $z$, due to a diameter variation at the same elevation.

ure. This plot clearly shows that, above the waterline, the three components balance with each other, causing the sensitivity to be close to zero; a closer look to the tower top, reveals that the sensitivity is positive there, while it is negative for the rest of the tower. Below the waterline instead, it shows that the most influential component is the hydrodynamic transfer function, $H_{a,0}$.

### Sensitivity of the Natural Frequency-dependent Component

The component $f(\omega_0)$ accounts for the effects of the resonant wave energy, the modal stiffness and the number of cycles, that are all related to $\omega_0$. Its contribution yields an overall reduction of the DEL, down to $-1\%$. Figure 3.7 shows the influences of its components: $\sqrt{S_{\zeta\zeta}(\omega_0)}$, $1/K_0$ and $\sqrt{(\omega_0)}$. From this figure, it is important to notice that an increase in diameter induces a small decrease of $f(\omega_0)$ at the very top of the tower, while it increases for the rest of the structure, approximately below $z = 128$ m. With Equation 2.12 in mind, this means that above $z = 128$ m the diameter enlarges the mass more than the stiffness, causing the natural frequency to decrease; vice versa, below $z = 128$ m the stiffness increases more than the mass, thus the natural

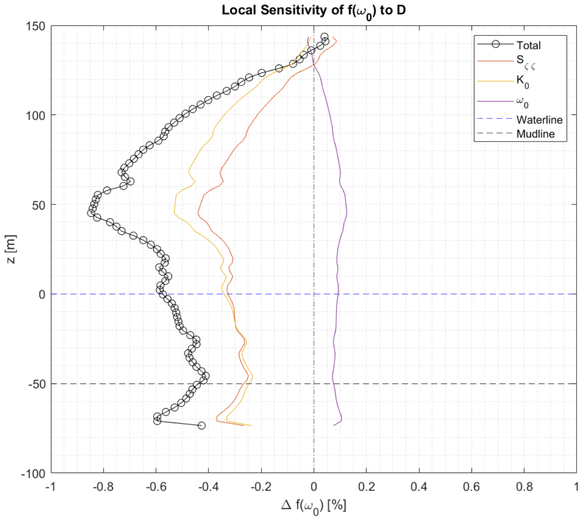

**Figure 3.7:** Local sensitivity of the function $f(\omega_0)$ and its components.

frequency increases. The other two components show a negative contribution to the sensitivity of $f(\omega_0)$, that mirrors the trend of the sensitivity to $\omega_0$. In particular, $K_0$ mirrors the effect of $\omega_0$ because it is proportional to the square of it, but it is at the denominator of $f(\omega_0)$; this suggests that, for the majority of the structure, increasing the diameter yields an increase in stiffness, thus a reduction in $f(\omega_0)$ and loads. $S_{\zeta\zeta}(\omega_0)$ instead, mirrors $\omega_0$ because an increase in diameter causes the natural frequency of the structure to move closer or further to the peak frequency of the wave spectrum, depending on the sign of the variation. Therefore, above $z = 128$ m, where the mass increases more than the stiffness, $\omega_0$ decreases and moves closer to the peak frequency, causing the structure to vibrate less frequently yet with greater amplitude, enlarging the loads. Vice versa, it increases below $z = 128$m.

### Sensitivity of the Hydrodynamic Transfer Function

The most significant contribution to the DEL sensitivity is given by the hydrodynamic transfer function $H_{a,0}$, as it is observed in Figure 3.6. The integration interval of $H_{a,0}$ ranges from the mudline to the waterline (see Equation 2.35), so the variations observed along the tower and below the mudline must be due to the natural frequency

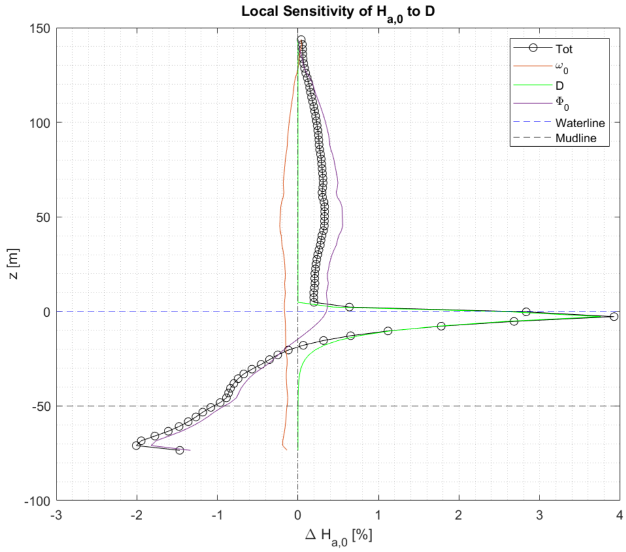

**Figure 3.8:** Local sensitivity of the hydrodynamic transfer function and its components.

and the modeshape, which are subjected to the diameter change also outside of the integration range of $H_{a,0}$. Figure 3.8 shows the components' contributions to the sensitivity, and thus confirms this behaviour. The plot shows a dependency from $\omega_0$ that is symmetrical to the sensitivity to the natural frequency previously observed in Figure 3.7. Note that also $C_M$ and $\eta_0$ implicitly depend on the natural frequency, so the plotted sensitivity to $\omega_0$ includes their influences as well. Hence, the combined contributions of $C_M$ and $\eta_0$ overcome the positive contribution of $\omega_0$, contributing negatively to the sensitivity of $H_{a,0}$.

Nevertheless, this contribution does not dominate the sensitivity, which is led by the modeshape $\Phi_0$ for the greater part of the structure, and by the diameter $D$ for the first 15 m below the waterline. A diameter increase below the waterline causes an increase in loads, since the integrand of the hydrodynamic transfer function depends on $D^2$; nevertheless, the sensitivity due to the diameter scales with the distribution function $\eta_0$ (see Figure A.3), therefore a peak is observed right beneath the waterline, that quickly drops to zero.

On the other hand, the modeshape $\Phi_0$ mainly determines the trend of the sensitivity of $H_{a,0}$ along the tower and below the water depth of 15 m. It is observed that an increase in diameter applied from the waterline to the top of the structure, causes a positive variation of $\Phi_0$ in the integration interval between mudline and waterline. The sensitivity becomes negative at $z = -15$ m; this means that the modeshape shows negative variations within the integration interval; this, weighted by $\eta_0$, yields a negative contribution to $H_{a,0}$. Figure 3.9 shows that, below $z = -15$ m the modeshape feels the non-local effects of the diameter change, that reduce its value. This behaviour is due to two main reasons; the first is that increasing the diameter at one elevation causes an increase in modeshape below it, and a decrease above; the second is that, the closer to the bottom the diameter is increased, the more negatively the modeshape varies. These trends are in line with what is expected, since adding diameter on the higher part of the structure favours the increase of mass, thus a more curved modeshape, while adding diameter on the lower part stiffens the structure and reduce the curvature of the modeshape.

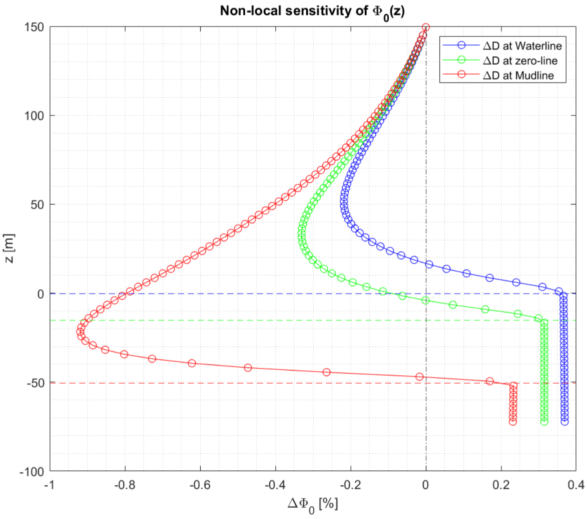

**Figure 3.9:** Non-Local sensitivity of the modeshape, due to a diameter increases at three different levels.

### Sensitivity of the Structural Transfer Function

Back to Figure 3.6, it is also interesting to analyse the local sensitivity of the structural transfer function, $H_{\mathrm{SH}}(z)$. This is plotted in Figure 3.10, that shows a sensitivity dominated by the contribution of the natural frequency, as previously explained. The particularity of $H_{\mathrm{SH}}(z)$ is that the lower bound of the integration interval changes for every point of evaluation of the DEL, i.e. it corresponds to the coordinate at which the transfer function is calculated, as shown in Equation 2.32. The sensitivity to the modeshape behaves similarly to what is observed for $H_{a,0}$, with the difference that, here, the switch from positive to negative sensitivity occurs at approximately $z = 40$ m, probably due to the different integration bounds. $\omega_0$ yields the biggest contribution to the sensitivity of $H_{\mathrm{SH}}(z)$, causing the same effect observed and explained above.

The contribution of the mass per length $\mu$, instead, is rather negligible compared to the other components. Its effect is only visible at the very top of the tower, where a small increment is observed. This behaviour is due to the nature of the integral's bounds, and to the modeshape. In fact, the variation of $\mu$ is only local and gets

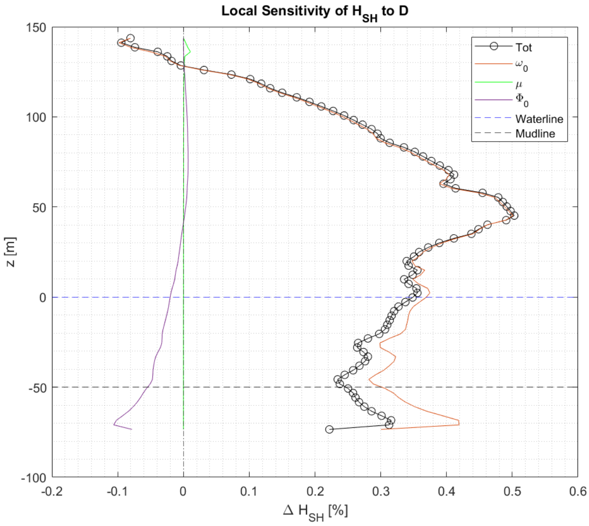

**Figure 3.10:** Local sensitivity of the transfer function $H_{\mathrm{SH}}$ and its components.

less and less significant, because going down the structure, the integration interval grows, and the modeshape tends to zero.

### 3.3.2 Non-Local Effects

A possible reason why the non-local effects are basically equal to the local ones is that some of the driving components of the DEL's sensitivity are constant along the height of the structure, and others are integrated over parts of it. The only component that may cause non-local effects that are different from the local ones, is the structural transfer function $H_{\mathrm{SH}}(z)$, because it varies along the vertical coordinate $z$. Nevertheless, it does not yield a significant contribution because the integral $\int_z^{z_{\mathrm{RNA}}} \Phi_0(\hat{z}) \cdot \mu(\hat{z}) \cdot (\hat{z} - z) \cdot d\hat{z}$ shows a relatively small sensitivity to the diameter change element-wise.

The surface in Figure 3.11 shows the non-local effects due to a variation of $D$ on $H_{SH}$. Here it is noticed that the non-local effects are actually more evident compared to what is observed in Figure 3.5, since the surface presents more curves along the

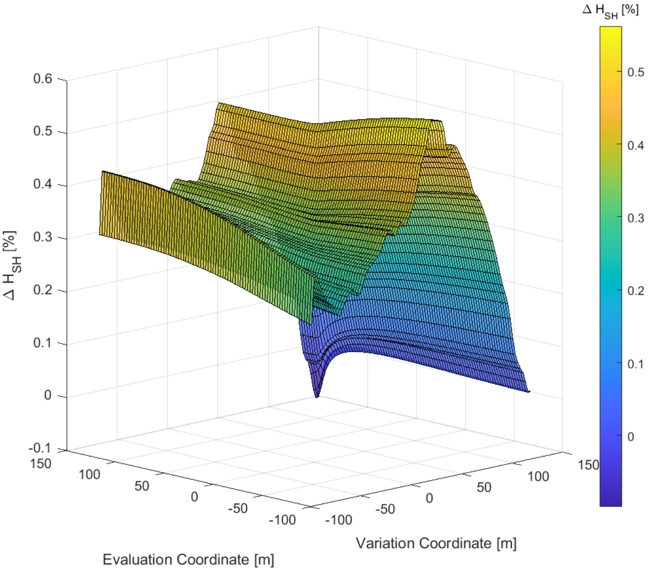

**Figure 3.11:** Sensitivity surface of the structural transfer function.

”Evaluation coordinate”; it also confirms that $H_{SH}$ is less sensitive to the diameter compared to $H_{a,0}$ of approximately one order of magnitude, since an increase of 5$\%$ in diameter causes a variation of the structural transfer function smaller than 0.6$\%$.

### 3.3.3 Hypotheses Discussion

Here, some of the hypotheses and choices taken throughout this chapter are discussed, aiming to speculate about how they may affect the results obtained. In particular, the hypotheses discussed concern the effect due to the choice of an average sea-state, the parked mode, and the fixity depth to model the soil stiffness.

#### Averaged Sea-states

According to the method adopted, only one sea state is considered, i.e. the average one. What if the wave-climate is different, and the average sea-state changes? The DEL varies proportionally to $\sqrt{S_{\xi\xi}(\omega_0)}$. Therefore, a sea-state whose spectrum's peak frequency is further away from the resonance frequency of the structure would induce lower loads, compared to a sea-state whose spectrum's peak frequency is closer to the resonant frequency. In general, the natural frequency is designed to be greater than the peak frequency of the wave spectrum. Therefore, accounting for a different sea-state would not yield qualitative changes in the sensitivity of $S_{\xi\xi}(\omega_0)$; nevertheless, the impact of the diameter variation through $\sqrt{S_{\xi\xi}(\omega_0)}$ on the sensitivity of DEL would change quantitatively, growing with the proximity of $f_p$ to $f_0$.

#### Parked Mode

In this thesis, the wind turbine is considered in parked mode, since the focus is on wave induced fatigue loads. It would be interesting, on the other hand, to study how the results would change if the energy production mode was considered. For example, how would the sensitivity of the wave induced DEL change, if a constant wind was exciting the structure? In this operational mode, the structural vibrations would be affected by the aerodynamic damping, and the response spectrum would include also the 1P and 3P frequency ranges, on top of the waves' one (see Figure 4.4). The increase in damping, could make the narrow-band assumption less valid. In this case, a method as that proposed by Dirlik would be needed to estimate the fatigue loads. The addition of 1P and 3P frequency ranges, on the other hand, would not affect the sensitivity significantly. In fact, the first natural frequency of the support structure is safely designed outside of these ranges, usually in the soft-stiff range as shown in Figure 4.4; therefore, the variation in natural frequency due to a local diameter change is not expected to move it into into these ranges, preventing an increase of DEL.

### Soil Model

Some observations can be done with respect to the choice of keeping the fixity depth diameter-independent. Considering the assumption of a diameter-dependent fixity depth, that thus increases with the monopile's diameter, how would the results be affected? It is important to mention that the diameter of the monopile is constant around the mudline, as can be seen in Figure A.1; thus, it is more significant to vary the diameter of all the elements belonging to this part of the monopile, instead of doing an element-wise variation. Two main factors shall be considered:

- The increase in diameter around the mudline;
- The increase in structural length;

The former causes a stiffening of the structure, and a negligible increase in wave loads, since it involves the lowest elements of the structure (see the sensitivity of the hydrodynamic transfer function $H_{a,0}$). The latter induces a decrease in stiffness, since longer structures are softer. Further calculations would be needed to understand exactly what contribution dominates the variation in stiffness; nevertheless, since the length of the varied portion of structure affects importantly the sensitivity of the DEL, it is expected that the diameter-induced stiffening would prevail on the increase of structural length, since a consistent part of the structure is involved ($\sim 50$ m). Thus, lower wave induced fatigue loads are expected, since the natural frequency would increase, shifting further away from the peak of the wave spectrum. Consequently, the sensitivity of the DEL around the mudline is expected to be more negative.

A more complete approach to account for soil stiffness, would be to remove the constraint on the horizontal displacement at the bottom, introducing springs along the underground part of the monopile, that contrast the horizontal displacement, as shown in Figure 3.12. If such model was considered, the FE model should be reformulated to account for the change of boundary condition at the bottom, and to include the springs in the stiffness matrix. The sensitivity analysis should be performed again, to investigate precisely what is the effect on the results. Moreover, it would be necessary to investigate if the springs stiffness depends on the diameter of the support structure, or if it reasonably independent. Nevertheless, it can be expected that a local variation of the diameter below the mudline, would not change the results qualitatively, since varying the diameter in the lower part of the structure is expected to increase its stiffness, and therefore reduce the loads.

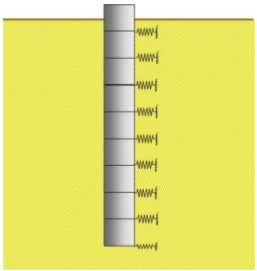

**Figure 3.12:** Representation of soil stiffness modeled with springs.

## 3.4 Conclusions

Here, the conclusions drawn from the sensitivity analysis are summarized.

With respect to the non-local effects, it was instead observed that they do not differ much from the local ones. This happens because the structural transfer function $H_{\mathrm{SH}}$, the component of the DEL that shows non-local effects, has a low impact on the global sensitivity of the DEL to the diameter.

Therefore, the following was concluded observing the local effects:

- **Throughout the tower**: the diameter does not have a significant effect on the wave induced fatigue load; only minor negative variations are observed.
- **Below the waterline**: more significant effects are observed. According to these, it is beneficial in order to obtain smaller loads, to reduce the diameter close to the waterline, due to the high influence of the wave kinematics. Note that this conclusion only relates to FLS design criteria. In fact, if ULS was considered, it should be expected that reducing the diameter would compromise the buckling stability of the structure.
- **Around the mudline**: the wave kinematics influence drops and the mode-shape takes the lead; this stiffens the structure and makes more beneficial an

increase to the diameter in the lower part of the support structure.

The numerical approach adopted to calculate the sensitivity, allowed to gather information about how the wave induced DEL depends on variations of the support structure's diameter, and to relate such information to the physics of the problem. Yet, this approach lacks an analytical description of the DEL sensitivity. In fact, analytical calculations allow to obtain more general results, in a quicker and more transparent way. Moreover, to determine what is the most beneficial support structure's diameter variation, it is necessary to know how the loads influence the structural design. Therefore, the analytical optimal support structure's diameter is calculated, aiming to achieve the lightest structure, respecting the constraint posed by the fatigue damage.

# Chapter 4

# Analytical Optimization

This chapter aims to describe an analytical approach to find the optimal support structure's diameter, i.e. the diameter that yields the lightest structure, able to withstand the wave induced fatigue damage. The pros of an analytical description are:

- **Intelligibility**: analytical equations are like open books, that show directly how the different quantities are related to each other. They allow to understand the whys and the hows of a certain result.
- **Speed**: the evaluation of an analytical equation is straightforward, and much faster than an iterative, numerical process.

On the other hand, the downside is that part of the completeness of the system description may be lost, if several simplifications are needed to follow an analytical approach. Indeed, equations often contain non-linear dependencies necessary to describe the complexity of the system, which may need numerical approaches to determine a solution. In other words, some completeness is lost, for the sake of intelligibility and speed.

The first section introduces the method developed to perform the analytical analysis, i.e. the equations and assumptions considered. Then, the results of such an analysis are presented along with the interpretation of the results, and a discussion of some relevant hypotheses.

## 4.1 Method

The method developed to find the analytical optimum is here presented. The case study, i.e. the model of the structure and wave climate used is first presented; then, the approach used to calculate the optimum design is explained in detail. Note that the method adopts a frequency domain approach.

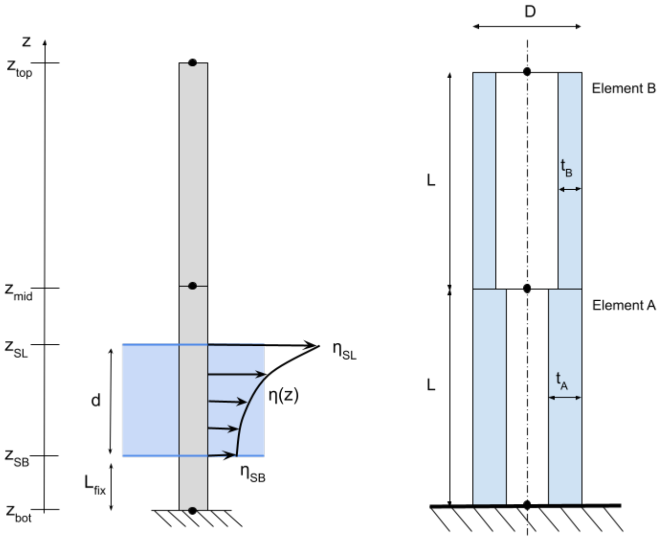

**Figure 4.1:** Representation of the FE model of the MP.

### 4.1.1 Case Study

To model the support structure, some simplifications were applied in favour of the transparency and ease of the calculations. The support structure was considered to have a constant diameter distribution and a "stepped" thickness distribution, where the elements' thickness are linearly related, as shown in Equation 4.2 and Figure 4.1. The RNA mass is neglected; thus, it is expected that the first modeshape has a smaller curvature, since the mass at the top is lower, and, due to a lower total mass, the first natural frequency is expected to be overestimated. To represent such structure an FE model was set up, characterized by:

- **Two Euler-Bernoulli beam-elements of equal length** $L$: each element is a hollow cylinder, and has constant diameter and thickness. Two elements were chosen for simplicity and to keep the equations transparent and lumped.
- **One DOF per node**: only the horizontal displacement was considered, i.e. the in-plane rotation $\phi$ and the vertical displacement $v$ were considered rigid.
- **Fixed bottom and free end**: the horizontal and rotational motion were as-

sumed fixed at the bottom, while they were set free at the top.

A graphical representation of this model is shown in Figure 4.1. To summarize:

$$D_A = D_B = D \tag{4.1}$$

$$t_A = \gamma \cdot t_B \tag{4.2}$$

where $\gamma$ is a constant parameter greater than 1, as it can be expected that the wall thickness of the bottom element is bigger than the one above, since the loads will be greater at the bottom, as the arm grows.

To obtain expressions in closed form of the fatigue damage, the thin wall assumption was taken, thus $t << D$. As a result, the area of the cross section (Equation 2.4) and second moment of area (Equation 2.5) of the $i$-th element became:

$$A_i \simeq \pi D_i \cdot t_i \tag{4.3}$$

$$I_i \simeq \frac{\pi}{8} D_i^3 \cdot t_i \tag{4.4}$$

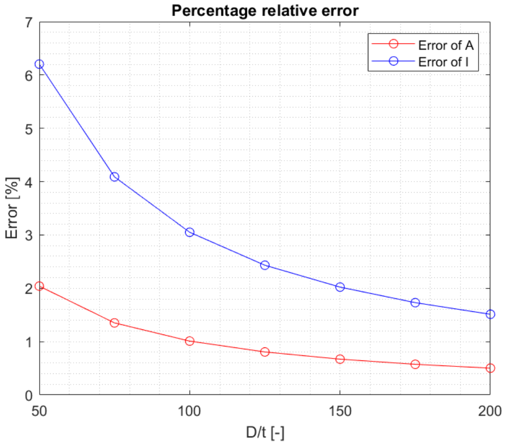

**Figure 4.2:** Relative percentage error of $A$ and $I$ due to the thin wall assumption.

Figure 4.2 shows the accuracy of the thin wall assumption when it is introduced in the equations of the area and second moment of area, with respect to the $D/t$ ratio.

It can be noticed that such an assumption is more accurate for elements characterized by a relatively big $D/t$ ratio.

For the structure described, the mass could be simply calculated as the sum of the masses of the two elements. Thus, accounting for the thin wall assumption, it returned:

$$M = M_A + M_B = \rho_s \cdot L \cdot (A_A + A_B) = \pi \cdot \rho_s \cdot L \cdot D \cdot (t_A + t_B) = \\ = \pi \cdot \rho_s \cdot L \cdot D \cdot (1+\gamma) \cdot t_B \tag{4.5}$$

### 4.1.2 Thickness

Equation 4.5 has a direct dependency on the diameter, but also an implicit one that lies in $t_B$. The thickness was computed so that it ”saturates” the fatigue damage. In other words, it was calculated as the smallest thickness that allows the support structure to withstand the cyclic loads during the time period considered. The fatigue damage was calculated according to Equation 2.26, considering the 1-Hz equivalent. Imposing the saturation of the fatigue damage, $F = 1$, for a period of $T_{\mathrm{LT}} = 2.5$ years, the wall thickness returned:

$$t = \frac{4}{\pi} \cdot \left(\frac{n_{\mathrm{eq}}}{a} \cdot T_{\mathrm{LT}}\right)^{\frac{1}{m}} \cdot \frac{\mathrm{DEL}}{D^2} \tag{4.6}$$

Therefore, the thickness that saturates the fatigue damage was obtained. Since the 1-Hz equivalent was used, $n_{\mathrm{eq}} = n_{\mathrm{ref,1Hz}} = T_{\mathrm{LT}}$. Equation 4.6 shows that the wall thickness is directly proportional to the DEL and it is inversely proportional to the square of the diameter. Thus, to allow the structure to accommodate a higher DEL, it was observed that it is more efficient mass-wise to increase the diameter rather than thickness, since, under the thin wall assumption, the mass scales linearly with both of them, while the DEL scales quadratically with the diameter.

### 4.1.3 Fatigue Load

As it is observed in equation 4.6, the thickness depends on the fatigue load that the structure experiences at a certain elevation. The DEL is the result of the actions of the environmental loads, such as waves and wind exciting the structure. More in general, it was assumed to be caused by two main contributions:

- A diameter-*dependent* contribution: $\mathrm{DEL}_{\mathrm{wave}}$

- A diameter-*independent* contribution: $\text{DEL}_{\text{D-ind}}$

To combine them, the damages due to these DELs were summed, since it was assumed that the two contributions occurred at different times; using Equation 2.26 yielded:

$$F = F_{\text{wave}} + F_{\text{D-ind}} = \frac{T_{\text{LT}}^2}{a} \cdot \left(\frac{\pi}{4} \cdot t \cdot D^2\right)^{-m} \cdot \left(\text{DEL}_{\text{wave}}^m + \text{DEL}_{\text{D-ind}}^m\right) \tag{4.7}$$

The total DEL was thus calculated as:

$$\text{DEL} = \left(\text{DEL}_{\text{wave}}^m + \text{DEL}_{\text{D-ind}}^m\right)^{\frac{1}{m}} \tag{4.8}$$

The two contributions are further analysed in the next sections.

### Wave Induced DEL

To calculate the DEL caused by the wave excitation, the frequency domain approach described in chapter 2, subsection 2.4.3 was used. Therefore, Equation 2.39, 2.35, 2.32 were considered.

Firstly, the modal quantities were determined, such as the natural frequency $\omega_0$, the modeshape $\Phi_0(z)$ and the modal stiffness $K_0$ of the first mode of vibration. For a FE model with 2 beam elements and 1 DOF per node, accounting for the clamped-bottom boundary condition, the mass and stiffness matrices are:

$$\mathbf{M} = \frac{\rho_s \cdot L}{420} \cdot \begin{bmatrix} 156 \cdot (A_A + A_B) & 54 \cdot A_B \\ 54 \cdot A_B & 156 \cdot A_B \end{bmatrix} \tag{4.9}$$

$$\mathbf{K} = \frac{12 \cdot E}{L^3} \cdot \begin{bmatrix} I_A + I_B & -I_B \\ -I_B & I_B \end{bmatrix} \tag{4.10}$$

These matrices were written based on the more general form presented in Equation 2.2 and Equation 2.1 respectively. Please, note that the the matrices and the vectors are flipped with respect to the vertical coordinate, e.g. the top of the structure is represented by the last row/element.

The results of the FE modal analysis, described in chapter 2, section 2.2, are presented here. Solving the characteristic polynomial of the system, yielded the first natural angular frequency:

$$\omega_0 = \beta \cdot D \tag{4.11}$$

Where $\beta$ is a constant, defined as:

$$\beta = \frac{\sqrt{105}}{L^2} \cdot \sqrt{E \cdot \frac{35 \cdot \left(1 - \sqrt{1+\gamma}\right) + 26 \cdot \gamma}{\left(595 + 676\gamma\right) \cdot \rho_s}}$$

Therefore, it was possible to see that the first natural frequency varies linearly with the diameter. The first modeshape, normalized by the maximum displacement resulted:

$$\Phi_0 = \begin{bmatrix} 0 \\ \frac{26(1+\gamma)-9\sqrt{1+\gamma}}{(1+\gamma)(-9+26\sqrt{1+\gamma})} \\ 1 \end{bmatrix} = \begin{bmatrix} \Phi_{0,\mathrm{bot}} \\ \Phi_{0,\mathrm{mid}} \\ \Phi_{0,\mathrm{top}} \end{bmatrix} \tag{4.12}$$

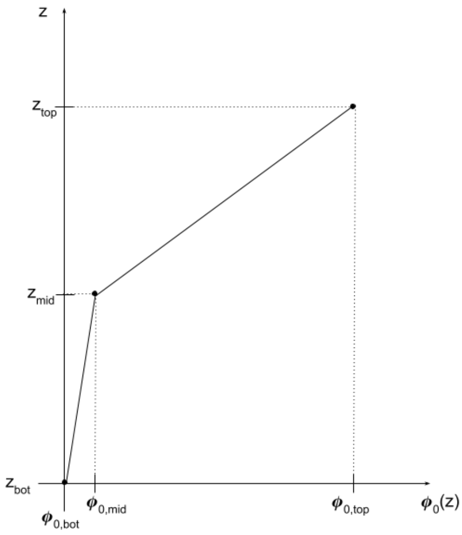

**Figure 4.3:** Graphical representation of the continuous and discrete modeshape.

Thus, the modeshape does not depend on the diameter, but only on the thickness ratio $\gamma$.

Since the integral in Equation 2.35 requires the modeshape evaluated at the sea level, $\Phi_0(z_{\mathrm{SL}})$, and seabed level, $\Phi_0(z_{\mathrm{SB}})$, these were computed interpolating linearly between the coordinates $[\Phi_{0,\text{bot}}; z_{\text{bot}}]$ and $[\Phi_{0,\text{mid}}; z_{\text{mid}}]$ (see Figure 4.3). The result of the interpolation is:

$$\begin{cases} \Phi_{0,\text{SL}} = \Phi_{0,\text{mid}} \cdot \frac{d+L_{\text{fix}}}{L} \\ \\ \Phi_{0,\text{SB}} = \Phi_{0,\text{mid}} \cdot \frac{L_{\text{fix}}}{L} \end{cases} \tag{4.13}$$

Where $L_{fix}$ is the fixity depth (see Figure 4.1).

The first modal stiffness was calculated as:

$$K_0 = D^3 \cdot t_B \cdot \delta \tag{4.14}$$

Where $\delta$ is a constant, defined as:

$$\delta = \frac{3\pi \cdot E \cdot \left[676\gamma^2 + \gamma \cdot \left(1901 - 1144 \cdot \sqrt{1+\gamma}\right) - 1225 \cdot \left(\sqrt{1+\gamma} - 1\right)\right]}{L^3 \cdot \left(1+\gamma\right) \cdot \left(9 - 26 \cdot \sqrt{1+\gamma}\right)^2}$$

It was observed that $K_0$ scales with the cube of the diameter, and linearly with the wall thickness of the element B.

To determine the analytical dependence of the hydrodynamic quantities on the diameter, the equations presented in section 2.3 were used, assuming deep water regime for the wave kinematics. This assumption is only valid if $d \cdot k_0 > \pi$, because in such case $\tanh(d \cdot k_0) \rightarrow 1$. Therefore, the dispersion relation became:

$$\omega_0^2 = g \cdot k_0 \tag{4.15}$$

From this equation it was possible to determine the wave number $k_0$ as a function of the diameter, substituting $\omega_0$ (Equation 4.11) into Equation 4.15:

$$k_0 = \frac{\beta^2 \cdot D^2}{g} \tag{4.16}$$

Please, note that the nomenclature of the wave number, small $k_0$, differs from that of the modal stiffness, capital $K_0$. Inserting the wave number into the distribution function, gave the following result for $\eta(z)$:

$$\eta(z) = \frac{\cosh\left(\frac{\beta^2}{g} \cdot D^2 \cdot (z - L_{\text{fix}})\right)}{\sinh\left(\frac{\beta^2}{g} \cdot D^2 \cdot d\right)} \tag{4.17}$$

The distribution function evaluated at the extremes of the integral in Equation 2.35, i.e. at water level and mudline, retuned:

$$\eta_{\mathrm{SL}} = 1 \tag{4.18}$$

$$\eta_{\mathrm{SB}} = \frac{1}{\sinh\left(\frac{\beta^2}{g} \cdot D^2 \cdot d\right)} \tag{4.19}$$

Note that for deep waters, at seabed the wave distribution function tends to zero, $\eta_{\mathrm{SB}} \to 0$.

The last hydrodynamic quantity worth mentioning is the inertia coefficient $C_M$, which for simplicity was kept constant:

$$C_M = 2 \tag{4.20}$$

Using this value of $C_M$ is a conservative choice, since, according to Equation 2.19, it is the maximum value of $C_M$. However, this is often considered a good assumption [23].

The wave energy is represented by the Pierson-Moskowitz spectrum. Inserting Equation 4.11 in Equation 2.16, the spectrum as a function of the diameter returned:

$$S_{\mathrm{PM}}(\omega_0) = \theta^2 \cdot D^{-5} \cdot \exp\left[-\psi^2 \cdot D^{-4}\right] \tag{4.21}$$

where the constants $\theta$ and $\psi$ are respectively:

$$\theta^2 = 0.3125 \cdot \left(\frac{2\pi}{T_P}\right)^4 \cdot H_S^2 \cdot \beta^{-5}$$

$$\psi^2 = 1.25 \cdot \left(\frac{2\pi}{T_P}\right)^4 \cdot \beta^{-4}$$

The mass per length $\mu$ is a quantity that depends on the cross section of a structure. It is therefore important to establish what is the mass per length of the middle node, as a discontinuity in the thickness occurs here. To account for this, it was chosen to calculate $\mu(z_{\text{mid}})$ as the the average of $\mu(z_{\text{bot}})$ and $\mu(z_{\text{top}})$. Thus:

$$\begin{cases} \mu_{\text{bot}} = \rho_s \cdot A_{\text{bot}} = \pi \cdot \rho_s \cdot D \cdot t_A \\ \\ \mu_{\text{top}} = \rho_s \cdot A_{\text{top}} = \pi \cdot \rho_s \cdot D \cdot \gamma \cdot t_B \\ \\ \mu_{\text{mid}} = \rho_s \cdot \frac{(A_{\text{top}}+A_{\text{bot}})}{2} = \pi \cdot \rho_s \cdot D \cdot \frac{1+\gamma}{2} \cdot t_B \end{cases} \tag{4.22}$$

It was then possible to determine DEL$_{\text{wave}}$. Inserting equations 4.22, 4.12, 4.11, into equation 2.32 returned the structural transfer function as a function of $D$:

$$H_{\text{SH}} = \pi \cdot (\beta D)^2 \cdot \rho_s \cdot D \cdot t_B \cdot L^2 \cdot \begin{bmatrix} 1 + \Phi_{0,\text{mid}} \cdot \frac{1+\gamma}{2} \\ \\ \frac{1}{2} \\ \\ 0 \end{bmatrix} \tag{4.23}$$

Considering then the hydrodynamic transfer function, and inserting the equations 4.20, 4.17, 4.13, and 4.11, into the equation 2.35, gave:

$$H_{a,0} = \frac{\pi}{4} \cdot \rho_w \cdot \beta^2 \cdot \frac{d}{L} \cdot \Phi_{0,\text{mid}} \cdot \Big(L_{\text{fix}} \cdot \eta_{\text{SB}} + L_{\text{fix}} + d\Big) \cdot D^4 \tag{4.24}$$

Inserting equations 4.24, 4.23, 4.21, 4.14, 4.12, and 4.11 into equation 2.39, and considering that in deep water regime $\eta_{\text{SB}} \to 0$, the equation of DEL$_{\text{wave}}$ gave:

$$\text{DEL}_{\text{wave}} = C_{\text{DEL,wave}} \cdot D^{\frac{9}{4}} \cdot \sqrt{\exp\left(-\psi^2 \cdot D^{-4}\right)} \tag{4.25}$$

Where:

$$C_{\text{DEL,wave}} = 1.8825 \cdot \frac{\pi^2}{8} \cdot \frac{\theta}{\delta} \cdot \xi_0^{-\frac{1}{2}} \cdot \beta^{\frac{19}{4}} \cdot \rho_s \cdot \rho_w \cdot C_M \cdot \tag{4.26}$$

$$\cdot\, d \cdot L \cdot \Big(d + L_{\text{fix}}\Big) \cdot \Phi_{0,\text{mid}} \cdot \begin{bmatrix} 1 + \Phi_{0,\text{mid}} \cdot \frac{1+\gamma}{2} \\ \\ \frac{1}{2} \\ \\ 0 \end{bmatrix}$$

### Diameter-independent DEL

There can be different sources of cyclic loading that are weakly or not at all related to the diameter of the structure. For example, if the wind load is considered, this can be seen as the result of two main contributions:

- **Thrust on the rotor**. This load depends on the wind conditions and the geometry of the blades, while it is independent from the geometry of the tower.
- **Drag on the tower**. This load not only depends on the wind conditions, but also on the geometry of the tower.

It is widely acknowledged that, in first instance, the thrust has a greater contribution than the drag force on the fatigue damage of the tower.

From a dynamic point of view, the diameter of the tower does not affect the spectrum of the wind induced excitation, such as the turbulence, 1P and 3P ranges, but it does affect the first natural frequency and modal stiffness of the structure. As a consequence, this has an effect on both the amplitude and the number of cycles of the loads that the structure experiences. On the other hand, it is true that usually the design philosophy chosen by the industry is to perform the tower design within the soft-stiff range of the response spectrum, where the first natural frequency is far from the peaks of the wind spectrum, as it can be seen in Figure 4.4.

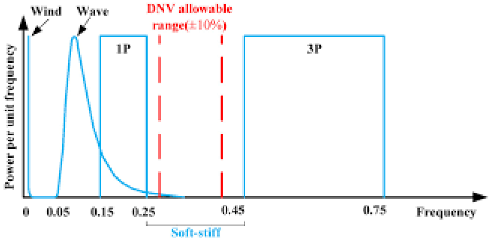

**Figure 4.4:** Example of spectrum of environmental loads of an offshore wind turbine [17].

Within this range, the oscillation of the structure does not vary significantly; it is therefore acceptable to consider the wind-induced fatigue loads independent from the diameter of the structure, as a first approximation. Therefore, if it was assumed that the diameter-independent DEL is due to the wind loads lumped at the top of the structure. Hence, it was written as:

$$\mathrm{DEL}_{\text{D-ind}} = \mathrm{DEL}_{\text{wind}} = \begin{bmatrix} \mathrm{DEL}_{\text{wind,bot}} \\ \mathrm{DEL}_{\text{wind,mid}} \\ 0 \end{bmatrix} \tag{4.27}$$

Since the DEL is an overturning moment, $\mathrm{DEL}_{\text{wind,bot}}$ and $\mathrm{DEL}_{\text{wind,mid}}$ were calculated as the DEL due to the wind thrust acting at the top of the structure, multiplied by the arm, i.e. $2L$ and $L$ respectively. Combining $\mathrm{DEL}_{\text{wave}}$ (Equation 4.25) with $\mathrm{DEL}_{\text{wind}}$ (Equation 4.27) as shown in Equation 4.8, the DEL was obtained.

Thus, it was possible to find the equation of the thickness as a function of the diameter, by inserting this result into Equation 4.6. Elevating $t$ to the $m$-th power, gave:

$$t^m = \left[ \frac{4}{\pi} \cdot \frac{1}{D^2} \cdot \left( \frac{T_{\text{LT}}^2}{a} \right)^{\frac{1}{m}} \right]^m \cdot \left( \mathrm{DEL}_{\text{wave}}^m + \mathrm{DEL}_{\text{wind}}^m \right) = t_{\text{wave}}^m + t_{\text{wind}}^m \tag{4.28}$$

Where $t_{\text{wave}}$ and $t_{\text{wind}}$ are respectively the thicknesses needed to withstand the wave loads and the wind loads.

$$\begin{aligned} t_{\text{wave}} &= \frac{4}{\pi} \cdot \frac{1}{D^2} \cdot \left( \frac{T_{\text{LT}}^2}{a} \right)^{\frac{1}{m}} \cdot \mathrm{DEL}_{\text{wave}} = \\ &= C_{t,\text{wave}} \cdot D^{\frac{1}{4}} \cdot \sqrt{\exp\left(-\psi^2 \cdot D^{-4}\right)} \end{aligned} \tag{4.29}$$

With $C_{t,\text{wave}}$ being a constant coefficient:

$$C_{t,\text{wave}} = \frac{4}{\pi} \cdot \left( \frac{T_{\text{LT}}^2}{a} \right)^{\frac{1}{m}} \cdot \begin{bmatrix} C_{\text{DEL,wave,bot}} \\ C_{\text{DEL,wave,mid}} \\ 0 \end{bmatrix} \tag{4.30}$$

On the other hand, the thickness needed to resist the wind loads was computed as:

$$t_{\text{wind}} = C_{t,\text{wind}} \cdot \frac{1}{D^2} \tag{4.31}$$

Where $C_{t,\text{wind}}$ is a constant coefficient defined as:

$$C_{t,\text{wind}} = \frac{4}{\pi} \cdot \left(\frac{T_{\text{LT}}^2}{a}\right)^{\frac{1}{m}} \cdot \text{DEL}_{\text{wind}} = \tag{4.32}$$

$$= \frac{4}{\pi}\left(\frac{T_{\text{LT}}^2}{a}\right)^{\frac{1}{m}} \cdot \begin{bmatrix} \text{DEL}_{\text{wind,bot}} \\ \text{DEL}_{\text{wind,mid}} \\ 0 \end{bmatrix}$$

Combining the two contributions, the thickness resulted:

$$t = (t_{\text{wave}}^m + t_{\text{wind}}^m)^{\frac{1}{m}} = \tag{4.33}$$

$$= \left[ \begin{bmatrix} C_{t,\text{wave,bot}}^m \\ C_{t,\text{wave,mid}}^m \end{bmatrix} \cdot D^{\frac{m}{4}} \cdot \left(e^{-\psi^2 D^{-4}}\right)^{\frac{m}{2}} + \begin{bmatrix} C_{t,\text{wind,bot}}^m \\ C_{t,\text{wind,mid}}^m \end{bmatrix} \cdot D^{-2m} \right]^{\frac{1}{m}}$$

From Equation 4.5, it was possible to see that the mass depends on the thickness $t_B$:

$$t_B = t_{\text{mid}} = \left[ C_{t,\text{wave,mid}}^m \cdot D^{\frac{m}{4}} \cdot \left(e^{-\psi^2 D^{-4}}\right)^{\frac{m}{2}} + C_{t,\text{wind,mid}}^m \cdot D^{-2m} \right]^{\frac{1}{m}} \tag{4.34}$$

Thus, inserting $t_B$ into Equation 4.5 gave:

$$M = \pi \cdot \rho_s \cdot L \cdot (1+\gamma) \cdot \tag{4.35}$$

$$\cdot \left[ C_{t,\text{wave,mid}}^m \cdot D^{\frac{5}{4}m} \cdot \left(e^{-\psi^2 D^{-4}}\right)^{\frac{m}{2}} + C_{t,\text{wind,mid}}^m \cdot D^{-m} \right]^{\frac{1}{m}}$$

Considering only the wave excitation in parked mode, Equation 4.35 became:

$$M = \pi \cdot \rho_s \cdot L \cdot (1+\gamma) \cdot C_{t,\text{wave,mid}} \cdot D^{\frac{5}{4}} \cdot \sqrt{e^{-\psi^2 D^{-4}}} \tag{4.36}$$

### 4.1.4 Inputs

To observe the behavior of mass with respect to the diameter, Equation 4.35 and Equation 4.36 were plotted. To do so, the values of the inputs were set for a specific case study, given by SGRE. This set of data is gathered in Appendix B, Table B.1.

In addition to these, it is important to specify also how the thickness ratio, $\gamma$, and the diameter-independent DEL, $\text{DEL}_{\text{wind}}$, were addressed.

#### Diameter-independent DEL

The magnitude of $\text{DEL}_{\text{wind}}$ was chosen arbitrarily, based on the magnitude of the wave induced DEL. To select a value that is not too big or too small compared to the wave induced DEL, the wind induced DEL was chosen within the range of the wave DEL. The load case shown in Figure 4.5 was then considered.

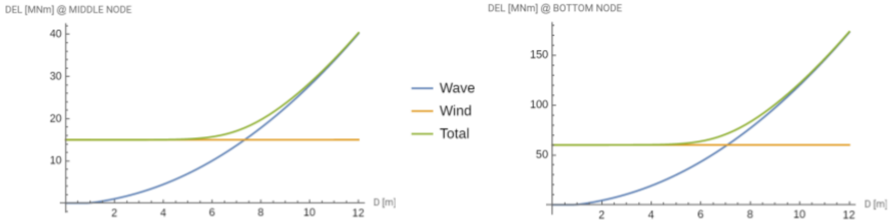

**Figure 4.5:** Representation of wave and wind loads combined, as shown in Equation 4.8.

#### Thickness Ratio

To perform the calculations as presented in the previous sections, it was necessary to fix the thickness ratio $\gamma$, otherwise one degree of indetermination would have remained. It was determined iteratively: after choosing an initial guess, the calculations were performed; then, the actual thickness ratio was calculated. This value was then used to perform the calculations again, until convergence. It was observed that, when only wave induced loads are accounted for, $\gamma \to 4.30$, i.e. the bottom element is more than four times thicker compared to the upper element.

When both loads were considered instead, $\gamma$ was observed to be a function of the diameter. Therefore, in this case $\gamma = 4.30$ was used as initial guess, and the function $\gamma(D)$ determined in the first iteration was then fed to the second iteration. Figure 4.6

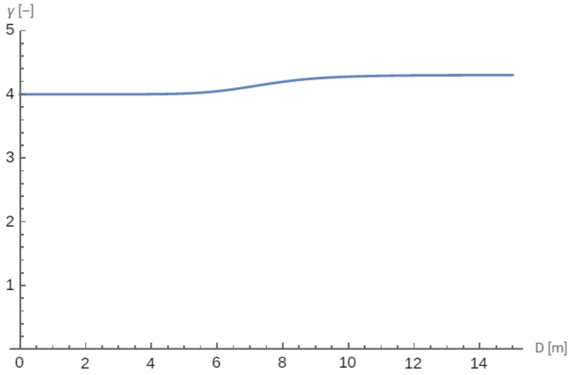

**Figure 4.6:** The thickness ratio as a function of $D$.

shows the plot of the function $\gamma(D)$ for the load case considered. This plot suggested that $\gamma$ is rather constant with respect to the diameter; only a slight increase was observed around $D = 7$ m, since in correspondence of this diameter the total DEL increases due to the wave loads.

## 4.2 Results and Discussion

Inputting the values listed in Table B.1, allowed to observe graphically the relation between the mass and the diameter.

### 4.2.1 Wave Loads Only

When only the wave induced loads were considered, it was observed that the mass grows almost linearly with the diameter, as it is shown in Figure 4.7. In the range $0 < D < 1$, the mass is approximately zero, due to the contribution of the exponential of $-1/D^4$. This is due to the energy of the resonant wave, that for small diameters is close to zero, as it is observed in Figure 4.8. Then, from $D \geq 1$, the trend is governed mainly by $D^{5/4}$, which explains why the mass increases almost linearly with the diameter. Therefore, accounting for resonant waves only yields the lightest structure for values of the diameter that tend to zero. On the other hand, for $D \to \infty$ the mass goes to infinity; in fact, regardless the spectral energy is almost zero for values of $D > 8$ m, the increase due to the diameter dominates with respect to the decrease of wave energy.

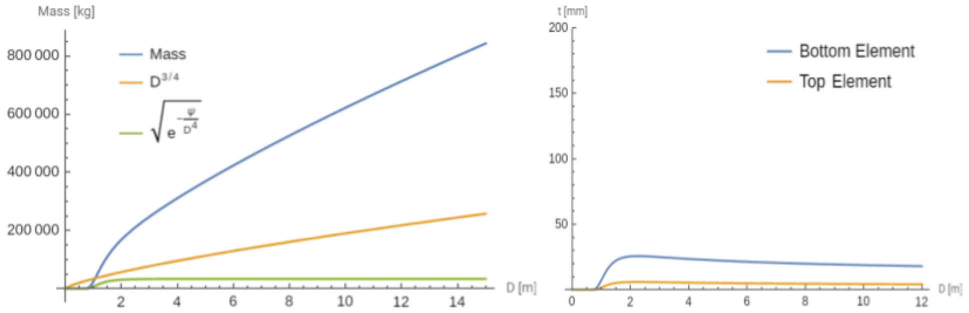

**Figure 4.7:** Mass and thickness vs. diameter for the case wave excitation only.

Despite these results, experience shows that the monopile-based support structures are not as slender (commonly the diameter ranges approximately between 5 - 12 m). Evidently, the assumptions taken into this approach fails to give a complete description of the system. As well as it can be expected that an excessively big diameter that may benefit fatigue resistance yields an excessively heavy support structure, it also makes sense that a too small diameter yields a light structure, yet not enough resistant to fatigue damage. On this line of thoughts, it was chosen to add a diameter-independent contribution to the DEL, a simple addition that aims to represent the contribution to fatigue damage of those factors that are not related to the diameter of the structure.

It is interesting to observe that there is a connection with the results of the sensitivity

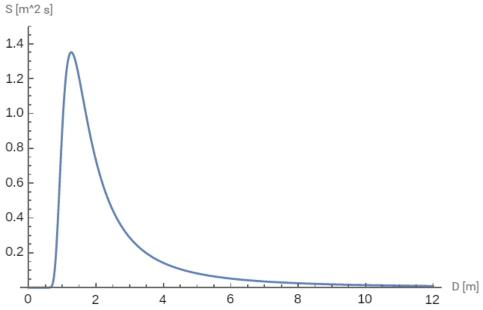

**Figure 4.8:** Spectral energy of the resonant wave vs. diameter.

analysis performed in the previous chapter. According to Equation 4.25, it can be derived that the sensitivity of the wave induced DEL is positive due to an increase in diameter, as it can be visualized in Figure 4.5. This aspect mirrors what is observed in Figure 3.6 below the waterline, where indeed the the sensitivity of DEL scales accordingly to the diameter. Therefore, in this simplified case study where the diameter varies by the same amount along the whole structure, it can be stated that the sensitivity of the wave induced DEL is dominated by the effect of the hydrodynamic transfer function.

### 4.2.2 Waves and Wind Loads

Including a diameter-independent component led to the equation of mass presented in Equation 4.35, whose trend can be seen in the following plot, for the load case of Figure 4.5. Note that in this case, the wind turbine is not anymore in parked mode; it would represent the power generation mode, i.e. when the wind turbine is rotating and the wind thrust acts at hub height. In this case, as shown in Figure 4.9, a different optimal diameter was found, depending on the load case considered. Table 4.1 shows the values found.

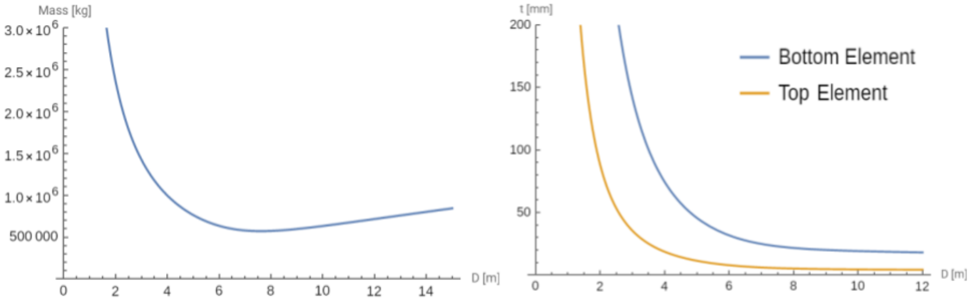

**Figure 4.9:** Mass and thickness vs. diameter for the case of waves and wind excitation.

**Table 4.1:** Optimal diameter and thickness for the load case considered.

| $\mathbf{DEL_{wind}}$ [MNm] | $\mathbf{D_{opt}}$ [m] | $\mathbf{t_{opt}}$ [mm] | **Mass** [ton] |
|---|---|---|---|
| [ 60.00 ; 15.00 ] | 7.55 | [ 22.80 ; 5.48 ] | 571.23 |

It was observed that, for $D > D_{\text{opt}}$ the mass grows, similarly to how it grows in the case of waves only, so it can be said that this part is dominated by the wave loads, that are diameter-dependent. For $D < D_{\mathrm{opt}}$, the trend is instead different, since for $D \to 0$, $M \to \infty$ . Therefore, this part of the plot is due to the diameter-independent contribution of the DEL. In fact, for $D \to 0$ in this case the thickness grows to infinity, and so does the mass.

Accounting for other load cases, allowed to understand how the optimal diameter changes with respect to the loads. Only the diameter-independent wind load was varied; the load cases considered, included a stronger one and a weaker one, compared to the one previously used. The results obtained per load case are gathered in Table 4.2 and Figure 4.10.

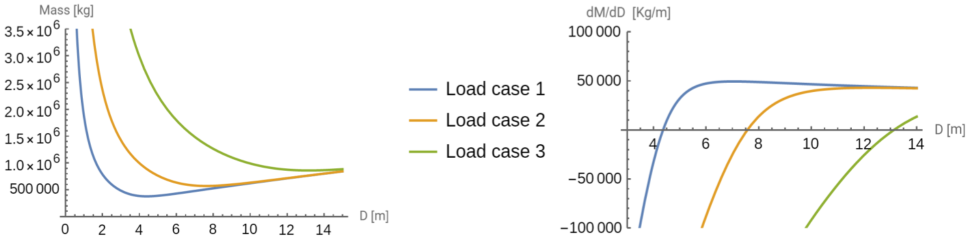

**Figure 4.10:** Mass vs. diameter (left) and first derivative(right) per load case.

**Table 4.2:** Results of the optimization per load case.

| $\mathbf{DEL_{wind}}$ [MNm] | $\mathbf{D_{opt}}$ [m] | $\mathbf{t_{opt}}$ [mm] | **Mass** [ton] |
|---|---|---|---|
| [ 20.00 ; 5.00 ] | 4.35 | [ 26.14 ; 6.28 ] | 377.44 |
| [ 60.00 ; 15.00 ] | 7.55 | [ 22.80 ; 5.48 ] | 571.23 |
| [ 180.00 ; 45.00 ] | 13.15 | [ 19.72 ; 4.72 ] | 859.84 |

It was observed that, increasing the load, the curves tend to widen, and to shift up-right. In other words, for the same diameter the mass increases with the loads, since a bigger thickness is needed to withstand them. Therefore, the optimal diameter shifts toward the right, supplying the structure with the required resistance, yet allowing a smaller wall thickness. Indeed, as mentioned above, to accommodate bigger loads, increasing the diameter is more beneficial compared to the thickness (see Equation 4.6). Nevertheless, the optimum also shifts upward, because the wave induced component of the loads scales quadratically with the diameter (see Equation 4.25). From the results obtained, it was possible to draw the line of the minima observed in Figure 4.11 (left figure) in function of the wind load. This shows how the optimal diameter behaves according to the wind load. Figure 4.11 (right figure) indicates that the optimal diameter grows with the wind loads, nevertheless it also suggests that the increase in diameter gets smaller for increasing wind loads.

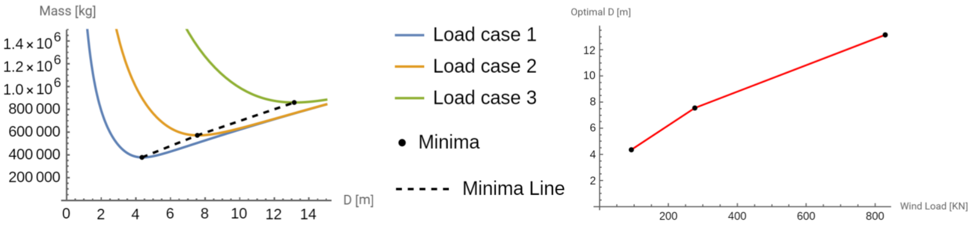

**Figure 4.11:** Line of the optima (left) and optimal diameter per load case (right).

### 4.2.3 Hypotheses Discussion

Here, some of the hypotheses and choices taken throughout this chapter are discussed, aiming to speculate about how they may affect the results obtained. In particular the thin wall assumption and the choice of neglecting the mass of the RNA are considered.

#### Thin Wall Assumption

As observed in Figure 4.2, the thin wall assumption's accuracy scales with the $D/t$ ratio: the bigger this is, the smaller is the error. In particular, the errors of the area and the second moment of area are smaller than $5\%$ for $D/t > 70$. Do the results obtained actually represent thin walled structures?

When waves only are accounted for, Figure 4.7 shows that $D/t \geq 70$ for every $D$. Therefore, it can be stated that in this case the thin wall assumption yields reasonably accurate results. When also the wind load is included, on the other hand, it is observed from Figure 4.9 that $D/t \geq 70$ for $D \geq 4.5$ m. Thus, the thin wall assumption is only reasonably accurate for diameters greater than 4.5 m. For smaller diameters, as explained above, the thickness grows exponentially and so does the $D/t$ ratio. In this case, the wall cannot be assumed thin, and the results observed have therefore a low accuracy. If the optimization was run for a non-thin walled structure for $D < 4.5$ m, it is expected that the results would change quantitatively, but not qualitatively. In fact, it physically makes sense that to withstand diameter-independent loads, a thick structure is needed if the diameter is small.

### Mass of RNA

For the sake of dealing with equations that show a clear and simple dependency on the diameter, the mass of the RNA was neglected. This is a rather extreme assumption, since an important part of the loads that the support structure needs to withstand comes from the RNA. So, how would the results change, accounting for $M_{\text{RNA}}$?

The RNA mass is implemented in the FE model, in particular in the element of the mass matrix that represents the top node of the top beam element:

$$\mathbf{M} = \frac{\rho_s \cdot L}{420} \cdot \begin{bmatrix} 156 \cdot (A_A + A_B) & 54 \cdot A_B \\ 54 \cdot A_B & 156 \cdot A_B + M_{\text{RNA}} \end{bmatrix} \tag{4.37}$$

Adding $M_{\text{RNA}}$, makes the relationship between the modal quantities and the diameter more complex,difficult to evaluate analytically; nevertheless, it can be expected that, compared to the assumption of $M_{\text{RNA}} = 0$:

- The natural frequency would be lower;
- The top of the modeshape would be relatively more displaced, compared to the middle node;
- The modal stiffness would result lower;

In fact, $M_{\text{RNA}}$ represents a lumped mass at the top of the structure, so it is expected to increase the mass of the system, and to decrease its overall stiffness.

Decreasing, the natural frequency is expected to move closer to the peak of the wave spectrum, thus increasing the wave induced fatigue loads. Consequently, the thickness needed to withstand such loads would increase accordingly, and so the total mass. The effect of the diameter-independent fatigue loads would be unaltered. Therefore, the results are not expected to change qualitatively. On the other hand, it can be expected to read greater values of mass on the vertical axis of Figure 4.7 and 4.9. Moreover, according to an increase of mass due to an increase in the wave induced fatigue loads, the right part of the curves in Figure 4.9 would shift upward, causing the optimal diameters to reduce, for all the load cases considered.

Last but not least, the expected increase in thickness would reduce the accuracy of the thin wall assumption, as explained above, since the $D/t$ ratio would globally reduce.

## 4.3 Conclusions

To summarize, in this chapter it is concluded that:

- Accounting for resonant waves only, a smaller diameter is always optimal. This is mainly due to the dependency of the wave induced fatigue load on the second power of the diameter, that cancels out the contribution of the thickness, that scales with the negative second power of the diameter. Therefore, the mass of the support structure scales with a positive power of the diameter, which yields a non-realistic optimum.
- Including a diameter-independent fatigue load, the lightest structure is not achieved at the smallest diameter, because it yields a massive thickness. Thus, the optimum found is more realistic compared to the case of waves only.
- The optimal diameter increases with the diameter-independent fatigue load; nevertheless, the amount by which it increases reduces with the loads.

# Chapter 5

# Conclusion

This final chapter aims to summarize the most relevant conclusions drawn from the results of the Sensitivity Analysis (Chapter 3) and the Analytical Optimization (Chapter 4), that are useful to answer the research question. After this summary, the intention is to propose some recommendations for future research, based on the lessons learnt throughout this thesis.

## 5.1 Conclusions

So, how does varying the support structure's diameter affect the wave induced fatigue loads of a monopile-based offshore wind turbine?

### 5.1.1 Sensitivity Analysis

The sensitivity analysis focused on the non-local effects on the wave induced fatigue load due to the variation support structure's diameter. These were calculated according to Seidel's approach to calculate the wave induced fatigue loads in frequency domain, therefore:

- Narrow-band response spectrum was assumed;
- Only resonant waves were accounted for;
- Only the first mode of vibration was considered;

A 2 DOFs FE model was developed and implemented to calculate the structural vibrations, according to the Euler-Bernoulli beam theory. The wave kinematics was assumed linear, and the wave loads were calculated with the Morison equation, neglecting the drag component. Performing a sensitivity analysis on a case study provided by SGRE, allowed to observe how the wave induced fatigue load behaves varying the diameter.

With respect to the local effects, three main conclusions were drawn. In particular:

- **Along the tower**: the diameter does not have a significant effect on the wave induced fatigue load; only minor negative variations are observed.
- **Below waterline**: more significant effects are observed below this. According to these, it is beneficial in order to obtain smaller loads, to reduce the diameter close to the waterline, due to the high influence of the wave kinematics.
- **Around mudline**: the wave kinematics influence drops and the modeshape takes the lead; this stiffens the structure and makes more beneficial an increase to the diameter in the lower part of the support structure.

With respect to the non-local effects, it was instead observed that they do not differ much from the local ones. This happens because the structural transfer function $H_{\mathrm{SH}}$, the component of the DEL that shows non-local effects, has a low impact on the global sensitivity of the DEL to the diameter.

### 5.1.2 Analytical optimization

The analytical optimization of the diameter for the lightest support structure aimed to give transparent insights on how the wave induce fatigue damage constrains the choice of the optimal diameter. The same case study was adopted, but the structural and hydrodynamic models were simplified. The thin-wall assumption was taken, and the mass of the RNA was neglected. Moreover, use was made of the deep water assumption for the wave kinematics. Two main load cases are considered: first the fatigue load is only wave induced, then a diameter-independent contribution associated with the wind loads is also accounted for, at different magnitudes.

The main conclusion drawn is that accounting for resonant waves only, a smaller diameter is always optimal. This is mainly due to the dependency of the wave induced fatigue load on the second power of the diameter, that cancels out the contribution of the thickness, that scales with the negative second power of the diameter. Therefore, the mass of the support structure scales with a positive power of the diameter, causing the observed trend.

## 5.2 Recommendations

In light of the insights obtained from the analysis conducted in this thesis, it is possible to state that it is relevant to deepen the understanding of how the support structure's diameter affects the wave induced fatigue loads of monopile-based offshore wind turbines. Nevertheless, the research question could be extended to: ”*How does varying the support structure's diameter affect the mass of a monopile-based offshore wind turbine, accounting for wave induced fatigue damage?*” In fact, although this thesis explains, through the sensitivity analysis, how varying the diameter of the support structure affects the wave induced fatigue loads, the other side of the medal is missing: how does varying the wave induced fatigue loads affect the design of the structure? As done in Equation 4.6, the thickness is designed as the minimum thickness capable of enduring the fatigue damage. Therefore, varying the DEL yields a variation of thickness, and consequently of mass as well. So, it is possible, starting from a variation in diameter, to compute what is the corresponding effect on the total mass of the support structure. This would allow to determine where it is beneficial to increase or decrease the diameter, considering *beneficial* a variation that reduces the fatigue loads, allowing the structure to be thinner and inducing an overall lighter support structure.

The analytical optimization offers some insights in this sense. Nevertheless, although it allows to see clearly what is the role played by the diameter in the wave induced DEL, and consequently in the fatigue constraint and the total mass, the simplifications adopted prevent the method from finding a realistic optimal design of the support structure, and to study in detail the non-local effects since the diameter varies constantly along the structure. Therefore, it is not an effective method to perform the structural optimization; a numerical approach shall be preferred instead, to achieve a detailed and realistically optimal design.

It may nevertheless serve as a simple method to understand the behaviour of the components involved in the process of optimizing the monopile-based support structures, since it is easy to keep track of the players involved. Moreover, some quick improvements for a more realistic optimization could be implemented. For example, the FE model can be ameliorated by including a second DOF, i.e. the in-plane rotation of the nodal sections, and also the mass and moment of inertia of the RNA; additionally the loads could be modelled better by considering a more accurate wind induced DEL, that accounts for a more detailed dependency on the support structure's diameter.

### Are the sensitivities obtained case sensitive?

It would be ideal to obtain insights on the wave induced DEL's sensitivity to the diameter, that are as much generic as possible. It would be therefore interesting to apply the methodology described in Chapter 3 to other case studies, to investigate to what extent the sensitivities obtained are case sensitive, and what features of the case studies have the most important impact.

### What if more modes of vibrations are included?

Only the first mode of vibration is considered, so the vibrations due to higher modes are neglected, and therefore the wave induced DEL is underestimated. More modes could be included to obtain a more accurate description of the structural dynamics. In fact, the sensitivity of the second mode could differ from that of the first mode, suggesting to perform different diameter variations. An approach to include the second mode is the following:

1. Perform the sensitivity analysis to get the natural frequency, the modeshape and the modal stiffness of the second mode of vibration;
2. Calculate the wave induced DEL according to Seidel's approach, simply using the modal quantities of the second mode of vibration in place of the first;
3. Combine the DEL due to the second mode of vibration with that due to the first mode;
4. Perform the sensitivity analysis;

It can be expected that the second mode has a lower impact on the DEL, compared to the first one. Nevertheless, it is not trivial to speculate qualitatively on such impact, which is the reason why it would be interesting to extend analysis, including at least the second mode of vibration.

# Appendix A

# Sensitivity Analysis

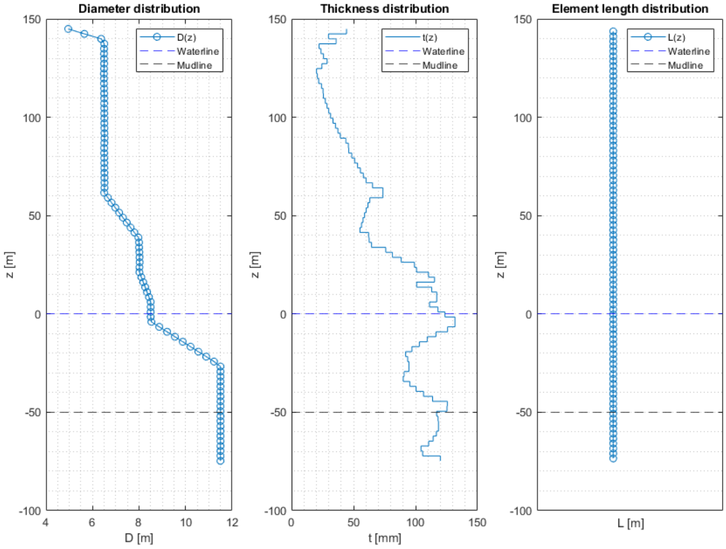

**Figure A.1:** Input diameter, thickness and element length distribution.

**Table A.1:** Input of the case study used in the sensitivity analysis.

| $\mathbf{M_{RNA}}$ [ton] | $\mathbf{I_{RNA}}$ [ton $\cdot$ m$^2$] | $\rho_{\mathbf{steel}}$ [kg/m$^3$] | **E** [GPa] |
|---|---|---|---|
| CONFIDENTIAL | CONFIDENTIAL | 7850.00 | 210.00 |

**Table A.2:** Wave climate used for the sensitivity analysis.

| Wind Speed [m/s] | $H_s$ [m] | $T_p$ [s] | Probability of Occurrence [%] |
|---|---|---|---|
| 1 | 0.43 | 6.56 | 2.47 |
| 2 | 0.48 | 6.53 | 3.30 |
| 3 | 0.53 | 6.50 | 4.66 |
| 4 | 0.59 | 6.47 | 6.04 |
| 5 | 0.65 | 6.45 | 7.23 |
| 6 | 0.73 | 6.43 | 8.03 |
| 7 | 0.82 | 6.42 | 8.53 |
| 8 | 0.93 | 6.42 | 8.68 |
| 9 | 1.06 | 6.44 | 8.39 |
| 10 | 1.20 | 6.48 | 7.58 |
| 11 | 1.36 | 6.55 | 6.66 |
| 12 | 1.54 | 6.65 | 5.70 |
| 13 | 1.73 | 6.78 | 4.71 |
| 14 | 1.92 | 6.93 | 4.05 |
| 15 | 2.13 | 7.10 | 3.36 |
| 16 | 2.35 | 7.29 | 2.65 |
| 17 | 2.56 | 7.48 | 2.06 |
| 18 | 2.78 | 7.68 | 1.65 |
| 19 | 2.99 | 7.87 | 1.25 |
| 20 | 3.20 | 8.05 | 0.92 |
| 21 | 3.41 | 8.22 | 0.65 |
| 22 | 3.60 | 8.39 | 0.49 |
| 23 | 3.79 | 8.55 | 0.34 |
| 24 | 3.97 | 8.70 | 0.22 |
| 25 | 4.14 | 8.85 | 0.13 |
| 26 | 4.30 | 9.00 | 0.08 |
| 27 | 4.46 | 9.15 | 0.06 |
| 28 | 4.62 | 9.31 | 0.04 |
| 29 | 4.78 | 9.49 | 0.03 |
| 30 | 4.95 | 9.70 | 0.02 |
| 31 | 5.13 | 9.96 | 0.01 |
| 32 | 5.35 | 10.30 | 0.01 |

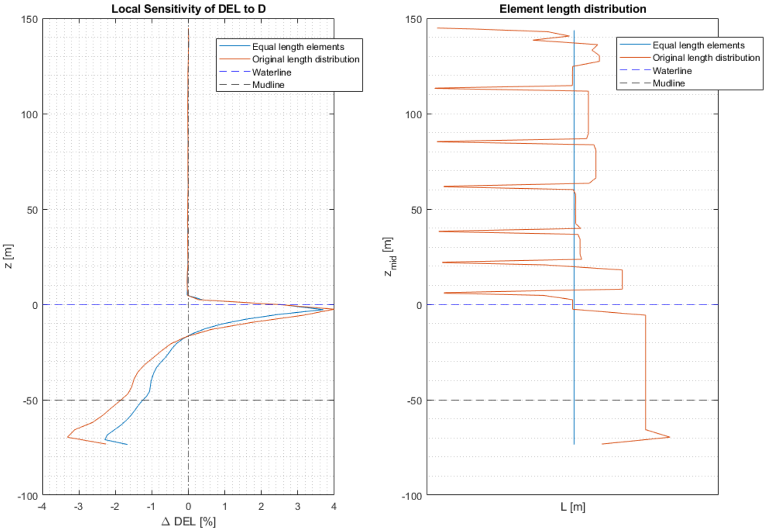

**Figure A.2:** Comparison between the sensitivity of DEL computed with the original length distribution vs. the rediscretized one.

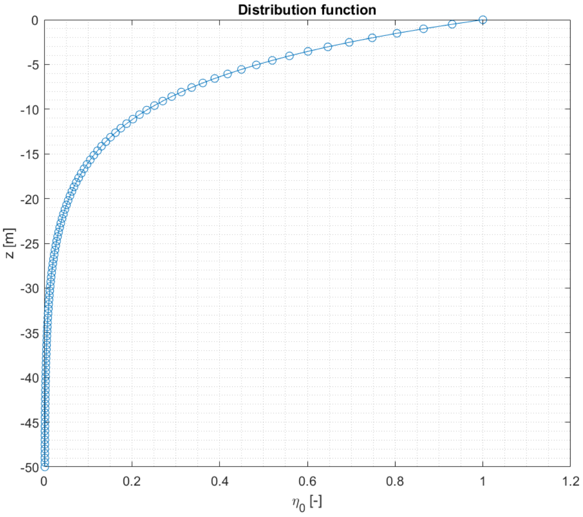

**Figure A.3:** Distribution function of the waves.

# Appendix B

# Analytical Optimization

**Table B.1:** List of the inputs used in the analytical optimization.

| **Quantity name** | **Symbol** | **Value** |
|---|---|---|
| Gravity acceleration | $g$ | 9.81 m/s$^2$ |
| Water depth | $d$ | 50.00 m |
| Critical damping | $\xi_0$ | 1.00 % |
| Fixity depth | $L_{\text{fix}}$ | 22.00 m |
| Element length | $L$ | 108.50 m |
| Significant wave height | $H_s$ | 4.00 m |
| Peak period | $T_p$ | 8.00 s |
| Density of steel | $\rho_s$ | 7850.00 kg/m$^3$ |
| Density of seawater | $\rho_w$ | 1025.00 kg/m$^3$ |
| Young modulus | $E$ | $2.10 \cdot 10^{11}$ N/m |
| Number of seconds in 2.5 year | $T_{\text{LT}}$ | $3600 \cdot 24 \cdot 365 \cdot 2.5$ s |
| Wohler exponent | $m$ | 4 |
| Intercept of mean S-N curve with the log(N) axis | $\log(a)$ | 13.75 |

# Bibliography

[1] Netherlands enterprise agency hollandse kust (zuid) - wind and water. `https://offshorewind.rvo.nl/cms/view/d2ab64a9-a87d-409f-92cc-15cd057b0e7d/wind-en-water-hollandse-kust-zuid`. Accessed: 2022-05-20.

[2] ASTM. Standard practices for cycle counting in fatigue analysis, 1985.

[3] N. Barltrop et al. Dynamics of fixed marine structures, 1991.

[4] K.-H. Chew et al. Fatigue sensitivity analysis of offshore wind turbine structures. 2015.

[5] K.-H. Chew et al. Optimization of offshore wind turbine support structures using an analytical gradient-based method. *Energy Procedia*, 80:100–107, 2015.

[6] T. Dirlik. Applications of computers in fatigue analysis phd dissertation, 1985.

[7] DNV-GL. Dnvgl:rp-c203: Fatigue design of offshore steel structures, September 2019.

[8] G. Flynn. Blueprint for offshore wind to green ireland's energy supply. `https://oceanfocus.ie/offshore-wind/`, July 2020.

[9] B.S. Gan. An isogeometric approach to beam structures. 1(1):225–226, 2018.

[10] P. Godfroy. Integrated design methodolohy for a monopile support structure for offshore wind turbines, using numerical optimization. *Master's thesis*, 2010.

[11] R. Haghi. Integrated design and optimization of an offshore wind turbine monopile support structure. *Master's thesis*, 2011.

[12] K.-H. Hapel. Festigkeitsanalyse dynamisch beanspruchter offshore-konstruktionen. (1), 1990.

[13] T. Haukaas. Euler-bernoulli beams. 2020.

[14] H. Jimin et al. Modal analysis, 2001.

[15] J.M.J. Journee et al. Offshore hydromechanics. pages 12–8, 2001.

[16] M. Kühn. Dynamics and design optimisation of offshore wind energy conversion systems. *Ph.D. Thesis*, 2001.

[17] W. Liao et al. Response of flexible monopile in marine clay under cyclic lateral load. *Ocean Engineering*, 147(1):89–106, 2018.

[18] N. Maljaars. Support structure optimization - on the use of load estimations for time efficient optimization of monopile support structures of offshore wind turbines, May 2017.

[19] P. Markolefas. Frequency domain fatigue analysis of offshore wind monopile support structure: For the purpose of offshore wind farm optimization. 2020.

[20] M. Muskulus. Dynamic response to irregular loadings. pages 150–151, 2020.

[21] Steelwind Nordenham. Beyond xxl – slim monopiles for deep-water wind farms, 2019.

[22] P. Ragan et al. Comparing estimates of wind turbine fatigue loads using time-domain and spectral methods. *WIND ENGINEERING*, 31(2):83–99, 2007.

[23] M. Seidel. Wave induced fatigue loads - insights from frequency domain calculations. *STAHLBAU*, 83(8):535–541, 2014.

[24] F. Sherrat et al. Predicting fatigue life from frequency domain data. *ENGINEERING INTEGRITY*, 18(1):12–16, 2005.

[25] T. Stehly et al. 2017 cost of wind energy review, September 2018.

[26] P. van der Male. Oe44135 - offshore wind support structures, 2020-2021.

[27] J. Van der Tempel. Design of support structures for offshore wind turbines. ph.d. thesis, 2006.

[28] Det Norske Veritas. Dnv-rp-c205: Environmental conditions and environmental loads, 2007.

[29] Det Norske Veritas. Dnv-os-j101: Design of offshore wind turbine structures, January 2013.

[30] L. Ziegler et al. Sensitivity of wave fatigue loads on offshore wind turbines

under varying site conditions. *Energy Procedia*, 80:193–200, 2015.

TU Delft Delft University of Technology

NTNU

SIEMENS Gamesa
RENEWABLE ENERGY